Case Studies in Thermal Engineering 75 (2025) 107015

Contents lists available at ScienceDirect

Case Studies in Thermal Engineering

journal homepage: www.elsevier.com/locate/csite

# Artificial intelligence - computational fluid dynamics study close contact melting of phase change materials in a finned shell-tube energy storage

Fathi Alimi [a], Nashmi H. Alrasheedi [b], Mohammad Edalatifar [c], Jana Shafi [d], Khalil Hajlaoui [b], Saleh Chebaane [e], Mohamed Bouzidi [e], Mehdi Ghalambaz [f,g,*]

[a] Department of Chemistry, College of Science, University of Ha'il, Ha'il, 81451, Saudi Arabia
[b] College of Engineering, Imam Mohammad Ibn Saud Islamic University (IMSIU), Riyadh, Kingdom of Saudi Arabia
[c] Laboratory on Convective Heat and Mass Transfer, Tomsk State University, Tomsk, 634050, Russia
[d] Department of Computer Engineering and Information, College of Engineering in Wadi Alddawasir, Prince Sattam Bin Abdulaziz University, 11991, Wadi Al Dawasir, Saudi Arabia
[e] Department of Physics, College of Science, University of Ha'il, P.O. Box 2440, Ha'il, Saudi Arabia
[f] Department of Mathematical Sciences, Saveetha School of Engineering, SIMATS, Chennai, India
[g] Refrigeration and Air Conditioning Technical Engineering Department, College of Technical Engineering, The Islamic University, Najaf, Iraq

ARTICLE INFO

*Keywords:*
Heat transfer enhancement
Liquid PCM flow
Phase change material
Close contact melting
Numerical simulation

ABSTRACT

The critical challenge of improving the latent-heat thermal energy storage (LHTES) efficiency was addressed in this study, as it is essential for advancing sustainable energy solutions. A new approach is proposed that uses heated liquid phase change materials (PCM) in direct contact with solid PCM to enhance the speed of thermal energy storage processes. Computational fluid dynamics and artificial neural networks were employed to examine the effects of various parameters on melting efficiency and temperature distribution. These parameters included PCM inlet pressures (5–15 Pa), inlet temperatures (311–359 K), hot water flow (HWF) inlet temperatures (311–359 K), HWF velocities (0.0067–0.0268 m/s), and the configuration of inlet/outlet ports. It was found that increasing HWF inlet temperature significantly accelerated the melting process. A case with the highest HWF inlet temperature (359 K), exhibited a remarkable 64.82 % improvement in melting rate compared to the baseline. Furthermore, optimization of PCM temperature and port configuration yielded approximately 30 % enhancement in system performance. It was concluded that higher inlet temperatures not only promoted more uniform melting but also significantly reduced melting time. The proposed method could substantially expedite melting and enhance heat transfer in LHTES systems.

## 1. Introduction

Latent Heat Thermal Energy Storage (LHTES) systems leverage phase change materials (PCMs) to absorb or release thermal energy

* Corresponding author. Department of Mathematical Sciences, Saveetha School of Engineering, SIMATS, Chennai, India
*E-mail addresses:* f.alimi@uoh.edu.sa (F. Alimi), nhrasheedi@imamu.edu.sa (N.H. Alrasheedi), m.edalatifar@gmail.com (M. Edalatifar), j.jana@psau.edu.sa (J. Shafi), kmhajlaoui@imamu.edu.sa (K. Hajlaoui), Chesaleh7@gmail.com (S. Chebaane), m.bouzidi@uoh.edu.sa (M. Bouzidi), ghalambaz.mehdi@gmail.com (M. Ghalambaz).

https://doi.org/10.1016/j.csite.2025.107015
Received 29 May 2025; Received in revised form 31 July 2025; Accepted 7 September 2025
Available online 11 September 2025

during phase transitions, typically from solid to liquid or vice versa. This capability enables LHTES to address mismatches between energy supply and demand by storing excess heat and releasing it when required [1]. One of the major applications of LHTES is in solar thermal systems, where PCMs help extend operational hours and improve thermal efficiency by maintaining stable temperatures during the charge/discharge cycles [2,3]. In building applications, PCMs are used for air conditioning and domestic hot water systems, adapting passively to ambient temperature fluctuations, thereby reducing energy consumption [4].

PCMs have also found relevance in hybrid systems such as photovoltaic thermal modules, where they enhance thermal management and energy conversion efficiency by cooling PV panels through latent heat absorption [5]. Cold thermal energy storage is another growing application area, utilizing PCMs to manage cooling loads efficiently in commercial and industrial systems [6].

The advantages of LHTES systems lie in their high energy storage density, near-isothermal operation, and compact design compared to sensible heat storage systems [7]. These systems do not require complex infrastructure like salt pumps or trace heating, making them cost-effective and easier to maintain [7]. Furthermore, PCMs enable thermal storage systems to be more sustainable, especially when integrated with recycled materials like Tetra Pak waste for forming composite PCMs, contributing to circular economy goals [3].

Despite the benefits, traditional PCMs face limitations due to low thermal conductivity and the risk of material leakage. To overcome these, innovations such as nano-enhanced PCMs, encapsulation, and shape-stabilized PCMs with porous supports (e.g., metal foams) are employed to improve thermal conductivity and structural integrity [1,8,9]. Hybrid enhancement strategies combining nanoparticles, fins, and metal foams have shown superior performance in heat transfer compared to single-technique solutions [9–11]. Geometric optimizations, like varying fin shapes or cavity inclinations, further optimize heat flow and melting behavior [12,13].

Despite the advantages, a primary limitation hindering the broader application of PCMs lies in their inherently low thermal conductivity [14]. This impediment necessitates the development of strategies to enhance heat transfer within PCM-based systems, ensuring uniform and rapid energy storage and release. Techniques such as the incorporation of nanoparticles [15], fins [16,17], and porous structures [18,19], and nano-encapsulation techniques [20,21] have been proposed to address this challenge. The effectiveness of fins in enhancing PCM thermal conductivity is well established, with scientists exploring various configurations to enhance the melting and solidification processes. Fins, with their simple design and ease of integration, offer a cost-effective means of augmenting heat transfer, with various configurations, including rectangular, circular, annular, and longitudinal types being explored [22,23].

Recent studies have underscored the significance of optimizing fin configurations for better thermal behavior of PCMs [24,25]. For instance, Almsater et al. [26] highlighted the dramatic speed up of solidification and melting achievable by optimizing fin counts in the vertical triplex-tube TES. Rathod and Banerjee [27] demonstrated the potential of longitudinal fins in improving heat transmission, leading to significant decreases in melting and solidification durations. These results underscore the crucial role of fin geometry and placement in maximizing LHTES thermal performance. The heterogeneity of melting rates across various regions of a TES unit, as observed by Mahdi et al. [28], further emphasizes the need for strategic fin arrangement to manage natural convection effectively. Yang et al. [29] advocated for a non-uniform distribution of annular fins, showcasing a substantial enhancement in melting uniformity and efficiency. Such empirical evidence illustrates the nuanced understanding required to exploit the full potential of fins in thermal management. Boujelbene et al. [30] revealed that in a horizontal triplex-tube configuration, arc-shaped fins significantly speed up the solidification process of PCMs. By fine-tuning the fin base's length and the angle between fins, the setup not only reduces the solidification time by 75 % but also boosts the heat recovery rate by 284 %, surpassing the performance of traditional longitudinal fins. Nidhal Ben [31] illustrated how incorporating circular Y-shaped fins into the vertical shell-tube design improves the melting efficiency of PCMs. By optimally adjusting the working fluid's temperature and Reynolds number, melting times are notably decreased—by 31 % with a higher Reynolds number and by 44 % when the temperature is increased, thereby highlighting the critical role of fin design and operational settings in enhancing thermal energy storage performance.

The interplay between PCM confinement and fin design has been explored, with studies by Ji et al. [32] and Jmal and Baccar [33] revealing the dual impact of fin number and length on melting. These insights point to a delicate balance between enhancing thermal transfer and avoiding adverse effects on the PCM's thermal behavior. Similarly, the comparative analyses conducted by Agyenim et al. [34], Mosaffa et al. [35], and Sciacovelli et al. [36] on different fin configurations elucidate the diverse ways through which fins can influence the efficiency and effectiveness of thermal storage systems. Through experimental and computational studies, these researchers have provided a comprehensive assessment of how circular and longitudinal fins, among others, distinctly impact the thermal efficiency of PCM-integrated systems. The advancements in fin technology, as evidenced by the innovative designs proposed by Patel and Rathod [37] and Al-Abidi et al. [38], pave the way for novel LHTES configurations that promise enhanced charging and discharging efficiencies.

In recent years, artificial neural network (ANN) analysis has been increasingly applied to LHTES systems to enhance their energy storage efficiency [39]. These studies aim to identify optimal values for various governing parameters such as flow rate, HTF temperature, and phase change rate to maximize system storage performance. Sultan et al. [40] employed an ANN model with over 7838 data points to investigate the impact of metal foam porosity on PCM melting time, revealing that a 7.5 % increase in porosity could reduce melting time by 66 %. Their study demonstrated ANN's efficiency in predicting melting volume fraction under various conditions and identifying optimal melting efficiencies. Thangapandian et al. [41] developed an ANN to predict thermal conductivity enhancement of Lauric Acid as PCM with copper oxide (CuO) and aluminum oxide ($Al_2O_3$) nanoparticles. Trained with experimental data, their ANN achieved low errors and high correlation coefficients, indicating accurate predictions of thermal conductivity enhancements across different conditions. Maalla et al. [42] utilized ANN models to predict melting durations for various fin configurations in a plate heat exchanger, leading to an optimal design that significantly reduced the time required for melting 70 % and 100 % of the PCM, demonstrating substantial improvement over systems without fins. These studies highlight the growing importance and

effectiveness of ANN in optimizing TES systems, paving the way for more efficient and responsive thermal energy storage solutions.

In parallel, the exploration of dynamic melting techniques represents a novel research direction, aiming to further improve the efficiency of LHTES systems. Unlike conventional heat transfer enhancement strategies, which often necessitate invasive modifications to the LHTES setup, thereby limiting the volume of PCM that can be effectively utilized, dynamic melting techniques offer a non-invasive and highly efficient approach to improving thermal performance. Dynamic melting techniques are predicated on the principle of inducing agitation or movement upon phase transition of the PCM. It is possible to achieve this movement through various mechanisms designed to maintain the PCM-to-LHTES volume ratio and maximize energy storage. These techniques are broadly categorized into four distinct groups: the application of ultrasonic vibrations, the utilization of twin-screw heat exchangers, the implementation of PCM flux tubes, and the recirculation of liquid PCM through external mechanisms [43,44].

The first strategy involves introducing ultrasonic vibrations within the LHTES system, which enhances the system's performance by preventing layers of solid PCM from forming within subcooled liquid PCMs [45,46]. In addition to enhancing the PCM's thermal conductivity, this approach also ensures uniformity in temperature distribution. The second strategy employs a twin-screw heat exchanger, wherein the surface that transfers heat is spun helicoidally for both discharge and charge processes, transferring the PCM through the heat exchanger area and maintaining it in a transportable state [47]. Furthermore, the concept of PCM flux, which involves carrying PCM across a heated surface via a transport tube, and the technique of dynamic melting, where liquid PCM is recirculated to control heat flow and transfer, represent the third and fourth strategies, respectively. This technique, often called dynamic ice melting or continuous mixing, involves the external circulation of liquid PCM to manage heat flow throughout the phase transition process [48].

Investigations into this dynamic approach, including those by He and Setterwall [49] and Tay et al. [50,51], have highlighted its efficacy in enhancing thermal conductivity and system responsiveness. Specifically, Tay et al. [51] demonstrated the method's capacity to double PCM system performance by recirculating melted PCM through a pre-melt tube and an additional pump, facilitating a more even and accelerated melting process. This reduced melting time and improved heat transfer significantly. Further analytical and experimental studies, such as those conducted by Gasia et al. [52], utilized two-dimensional Cartesian simulations to explore the intricacies of this phenomenon. These studies confirmed that the velocity of PCM circulation exerts a substantial impact on melting duration, thermal efficiency, and progress of the front of melting and temperature profiles within the storage system. Higher velocities were found to enhance the process, indicating that the benefits of dynamic melting are more pronounced with increased PCM movement than with alterations of the working fluid's velocity.

As a result of these studies, it was demonstrated that dynamic PCM recirculation techniques can significantly enhance the storage efficiency of latent-heat TES systems. These methods promise significant improvements in thermal management by optimizing PCM flow parameters, offering a robust solution to the challenges traditionally associated with PCM-based energy storage. The integration of dynamic melting with fin-assisted heat transfer mechanisms presents a more promising hybrid enhancement strategy, offering potential synergies that could significantly boost LHTES thermal efficiency. The exploration of hybrid enhancement strategies, combining the benefits of fin integration with dynamic melting, presents an innovative method of augmenting the thermal response of

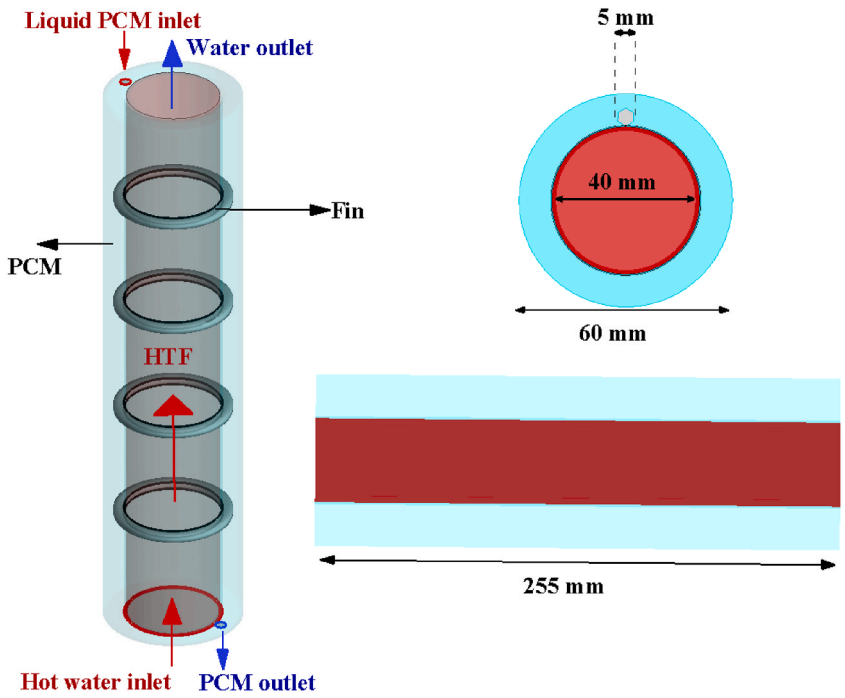


**Fig. 1.** Schematic representation of the initial design of the cylindrical cylinder's TES along with fins and molten PCM input and output ports.

PCM-based systems, which is the aim of the present study.

This research presents a comprehensive investigation into the dynamic melting of PCM in a finned shell-tube heat exchanger, employing an innovative model of CFD simulation and ANN technique. The study explores, for the first time, the complex interplay between various operational parameters including PCM inlet pressure and temperature, working fluid conditions, and port configurations in a finned LHTES unit. By integrating dynamic melting techniques with fin-assisted heat transfer, this work introduces a novel hybrid enhancement strategy that promises significant improvements in thermal efficiency. The use of ANN modeling alongside traditional CFD simulations offers a unique approach to analyzing and predicting system performance across a large range of conditions, providing valuable insights for the optimization of LHTES systems.

## 2. System overview and theoretical structure

### 2.1. System description

High-temperature water fills an inner cylinder, surrounded by an outer cylinder holding PCM. Copper tubes, depicted in Fig. 1, enhance heat exchange between water and PCM. Hot water passes through a pipe to transfer heat to a copper wall, which is then transferred to PCM. Hence, the PCM absorbs the water heat and changes its phase by satisfying melting conditions. Hot water continuously enters the pipe from one side to maintain stable conditions, then exits at the end surface after passing through the pipe's length. This article introduces a new method for using fins and hot melt PCM simultaneously. Fig. 1 illustrates surfaces near the hot water inlet and outlet, enabling molten PCM to flow in and out of the outer cylinder. The initial design directs water and PCM to exit in opposing directions. The diameters of the inner and outer pipes, PCM ports, and pipe lengths are 20, 60, 5, and 255 mm, respectively. Such LHTES systems are applicable in power plants and industrial waste heat recovery, where they can provide a constant flow of liquid PCM.

The following study examines variables including velocity, pressure, and temperature of the inlets, as well as the number of PCM ports. Additionally, two different PCM flow models without PCM ports and with molten PCM flow have been developed and compared with the basic geometry to determine how dynamic melting impacts PCM flow. Some cases investigate gravity's effect on this mechanism by altering the direction of entry and exit of water and PCM; The direction of entry and exit can be either in or against gravity's direction. The thermophysical data of the materials employed in the current study are summarized in Table 1. This study examines the properties of PCM RT35 from Rubitherm GmbH, Germany, employed as the energy storage medium, alongside copper utilized in the fins and water tube walls. RT35, an organic paraffin-based phase change material, offers high latent heat capacity and a melting point around 35 °C, ideal for thermal storage. Copper, chosen for its excellent thermal conductivity and durability, enhances heat transfer between the water and PCM, optimizing the system's efficiency.

### 2.2. Mathematical formulation

For the described model, heat transfers and forced convection flows within hot water flow (HWF) in tubes are considered, along with mixed convection flows into PCM chambers and the transfer of heat tube walls. Various assumptions are considered in this work, including incompressibility, laminarity, transientity, and unsteadiness. Gravity is viewed in the z-axis orientation. Suitable insulations are assumed at the perimeters of solids, and no-slip boundary conditions are assumed for solid edges.

In the case of HWF and PCM flow, mass conservation is explained as follows [53,58,59]:

$$\frac{\partial U_j}{\partial x_j} = 0 \tag{1}$$

where $U$ is the fluid velocity and $x$ denotes the spatial coordinate. HWF's equations for energy conservation and momentum are the following:

$$\frac{\partial T}{\partial t} + U_j \frac{\partial T}{\partial x_j} = \alpha_{HWF} \frac{\partial^2 T}{\partial x_j \partial x_j} \tag{2}$$

**Table 1**
Copper and RT35 thermophysical properties.

| Properties | | RT35 [31,53,54] | Copper (inner tube wall and fin) [55,56] | Water [56,57] |
|---|---|---|---|---|
| Mean density | $\rho_{PCM}$ (kg/m$^3$) | 815 | 8900 | 997.1 |
| Viscosity | $\mu_{PCM}$ (kg/m.s) | 0.023 | – | 0.000957 |
| Specific heat | $C_p$ (J/kg.K) | 2000.0 | 386 | 4179 |
| Conductivity coefficient | $k$ (W/m.K) | 0.20 | 380 | 0.613 |
| Latent heat | $h_L$ (J/kg) | 160000 | – | – |
| Temps at solidus | $T_{PCM_{solid}}$ (K) | 305 | – | – |
| Temps at Liquidus | $T_{PCM_{liquid}}$ (K) | 311 | – | – |
| Thermal volume expansion | $\beta$ [1/K] | 0.0006 | – | 0.00021 |

$$\rho_{HWF}\left(\frac{\partial U_i}{\partial t}+\frac{\partial\left(U_iU_j\right)}{\partial x_j}\right)=-\frac{\partial P}{\partial x_i}+\mu_{HWF}\frac{\partial}{\partial x_j}\left(\frac{\partial U_i}{\partial x_j}+\frac{\partial U_j}{\partial x_i}\right) \tag{3}$$

here, $P$ refers to pressure, $U$ is the fluid velocity, $T$ corresponds to static temperature, $t$ corresponds to flow time, and $\alpha$ is thermal diffusivity coefficient, $\rho$ is the density, μ is the dynamic viscosity, and $g$ is the gravity acceleration. The subscript HWF indicates the water as the working fluid. Formulas for energy preservation in solid copper fins and sturdy copper middle barriers are outlined below:

$$\frac{\partial T}{\partial t}=\alpha_{copper}\frac{\partial^2 T}{\partial x_j\partial x_j} \tag{4}$$

The subscript of copper indicates the copper tube and fins. The Boussinesq approach is applied to describe the momentum equations governing PCM flow, as detailed below [60]:

$$\rho_{PCM}\left(\frac{\partial U_i}{\partial t}+\frac{\partial\left(U_iU_j\right)}{\partial x_j}\right)=-\frac{\partial P}{\partial x_i}+\mu_{PCM}\frac{\partial}{\partial x_j}\left(\frac{\partial U_i}{\partial x_j}+\frac{\partial U_j}{\partial x_i}\right)+\rho_{PCM}g_i\beta_{PCM}\left(T-T_{ref}\right)+S_i \tag{5a}$$

where using the given parameters, $T_{ref}$ (reference temperature) refers to 293 K, and $\beta$ is the thermal expansion coefficient, the subscript PCM denotes the PCM material. Influences from phase shifts in the momentum formula are accounted for by inserting a Darcy's law resistance component, termed a source factor [61]:

$$S_i=\frac{(1-\Omega)^2}{\left(\varepsilon+\Omega^3\right)}U_iA_{mushy} \tag{6}$$

in which $\Omega$ is the liquid fraction field. The mushy zone parameter, $A_{mushy}$, is a fixed value between 1E4 Pa·s/m$^2$ and 1E7 Pa·s/m$^2$, typically called the mushy region constant. In this research, we set it at 1E5 Pa·s/m$^2$ [16,53]. Additionally, $\varepsilon$, a small number (0.001), is used to avoid division by zero. The liquid portion fraction ($\Omega$) is determined using the following method [61,62]:

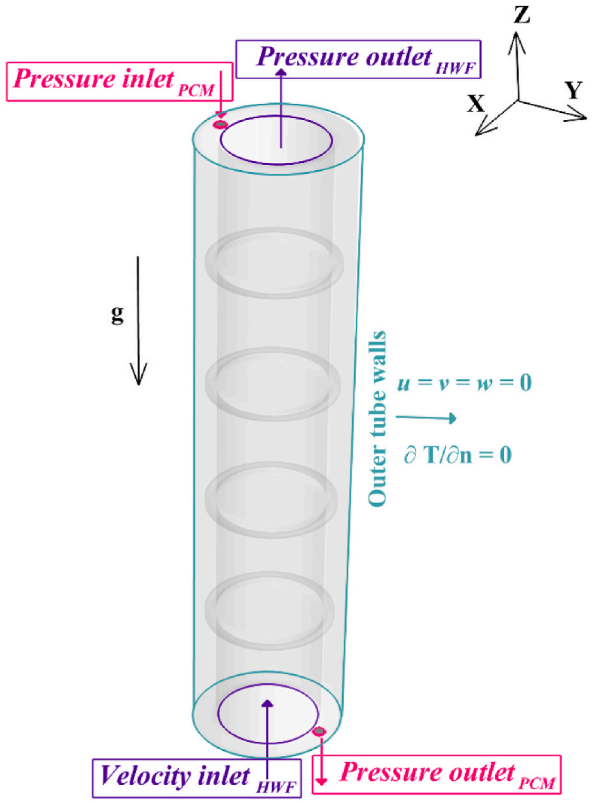


**Fig. 2.** Open latent-heat TES unit boundary conditions.

$$\Omega = \begin{cases} 0 \quad \text{if } T < T_{PCM_{solid}} \\ \dfrac{T - T_{PCM_{solid}}}{T_{PCM_{liquid}} - T_{PCM_{solid}}} \quad T_{PCM_{solid}} < T < T_{PCM_{liquid}} \\ 1 \quad T > T_{PCM_{liquid}} \end{cases} \tag{7}$$

here, subscripts of solid and liquid refer to the solid and liquid status of the PCM material, respectively. The energy conservation for PCM flow can alternatively be derived as outlined below [53]:

$$\frac{\partial}{\partial t}(\rho_{PCM_m} H_T) + U_j \frac{\partial\left(\rho_{PCM_{Liquid}} H_T\right)}{\partial x_j} = \frac{\partial}{\partial x_j}\left(k_{PCM_m} \frac{\partial T}{\partial x_j}\right) \tag{8}$$

As described below, $H_T$, representing total enthalpy, is computed by summing sensible enthalpy ($h_S$) and latent heat ($h_L$).:

$$H_T = h_S + \Omega h_L \tag{9}$$

Additionally, the thermophysical properties of PCM, such as thermal conductivity, vary with the liquid fraction and can be evaluated as follows:

$$k_{PCM_m} = \Omega k_{PCM_{Liquid}} + (1 - \Omega) k_{PCM_{Solid}} \tag{10}$$

### 2.3. Defining boundaries

Fig. 2 illustrates the conditions for the boundaries that are related to the proposed geometry.

- The HWF is entered with $T_{in,HWF}$ and velocity of $w_{in,HWF}$. It is considered that convection flow is established at the outlet of the HWF tube:

$$\text{condition}\begin{cases} \text{Inlet} \rightarrow w = w_{i,HWF} \quad \text{and} \quad T = T_{i,HWF} \\ \text{Outlet} \rightarrow \ P_{O,HWF} = 0, \text{and} \ \dfrac{\partial T_{O,HWF}}{\partial z} = 0 \end{cases}^{\text{HWF}} \tag{11}$$

- PCM flows into the enclosure at a high temperature and exits at zero gauge pressure:

$$\text{conditions}\begin{cases} \text{Inlet} \rightarrow P = P_{i,PCM} \quad \text{and} \quad T = T_{i,PCM} \\ \text{Outlet} \rightarrow \ P = 0, \text{and} \ \dfrac{\partial T_{i,PCM}}{\partial z} = 0 \end{cases}^{\text{PCM ports}} \tag{12}$$

- The latent heat thermal energy storage units are designed to be well insulated to prevent heat loss. Heat losses over long periods can be an issue; however, the present study investigated the charging behavior of the unit during the charging process. The charging process takes about 3 h. During this time, the heat losses are negligible, and thus a zero-heat flux boundary condition can be assumed for the shell boundaries. The phase change material is also in direct contact with the tube and fins; therefore, contact resistances can be neglected. Thus, a well-insulated enclosure with zero heat-flux, non-slip, non-permeability boundary conditions is introduced as:

$$\text{conditions}\begin{cases} v = u = w = 0 \\ \dfrac{\partial T}{\partial n} = 0 \end{cases}^{\text{Outer tube walls}} \tag{13}$$

- At the beginning, the domain is initially cold with a temperature of $T_{ref}$ and a velocity and pressure of zero:

$$\text{condition}\begin{cases} T_{PCM} = T_{HWF} = T_{ref} = 293K \\ v = u = w = 0 \\ P_{PCM} = 0 \end{cases}^{\text{Initial domain}} \tag{14}$$

## 3. Numerical method and validation

Numerical methods, grid sensitivities, and a literature study validation are discussed in this section.

### 3.1. Solver procedure process

A pressure-velocity coupling methods was implemented to tackle equations governing mass, energy, and momentum conservation. For calculating derivatives of the variables, a least squares approach at the cell level was applied. The QUICK method handled the approximation of differential terms within the momentum and energy equations. Pressure adjustments relied on a method termed PRESTO. Relaxation coefficients were assigned values of 0.1 for both pressure and momentum, while energy received a coefficient of 0.6. Convergence limits were established at 1E-4 for continuity and momentum, and a stricter 1E-6 for energy. The computation halts when the melted volume fraction hits 0.999, marking the point where the PCM becomes entirely liquefied. Following this, a detailed examination and validation of the grid are outlined in the next section.

### 3.2. Independency process for grids

By adjusting grid size, the research evaluates the effect of grid granularity on the precision of computational outcomes. As a reference case, $w_{WTF_{in}} = 0.0135$ m/s, $T_{WTF_{in}} = 323$ K, $P_{PCM_{in}} = 10$ Pa and $T_{PCM_{in}} = 323$ K was selected, and an analysis of the grid was conducted for this setup. Fig. 3 depicts a time history of melting fraction (MVF) for various grid sizes. As a result, the grid case with NC = 2,430,000 was adopted for all computations in this research. Increasing the grid size from 2,430,000 to 2,530,000 does not affect the results. Fig. 4 depicts the overall grid as well as detail sections used in the current study.

The results were verified as independent of time step size. Simulations were conducted using four distinct time steps: 0.2, 0.1, 0.05, and 0.025 s, with a grid count of 2,430,000. As indicated in Table 2, substantial temperature and melting fraction differences were observed for time steps larger than 0.05 s. However, the discrepancy between results obtained with 0.05 and 0.025 s time steps was negligible. Consequently, to optimize computational efficiency and reduce simulation time, time steps of 0.05 s were chosen.

### 3.3. Validation

To validate the precision of the current simulation, reference was made to the findings of Kamkari et al. [63], who conducted experiments within a vertically oriented rectangular enclosure containing paraffin wax, dimensions 50 mm wide and 120 mm tall. The investigation focused on analyzing heat transfer during the wax's melting phase. The enclosure was constructed with all surfaces insulated to block heat loss, except for the left vertical wall, which received uniform heating. Temperature changes within the enclosure were tracked using an array of thermocouples. The initial state saw the wax at 25 °C, in contrast to the heated wall's temperature of 70 °C.

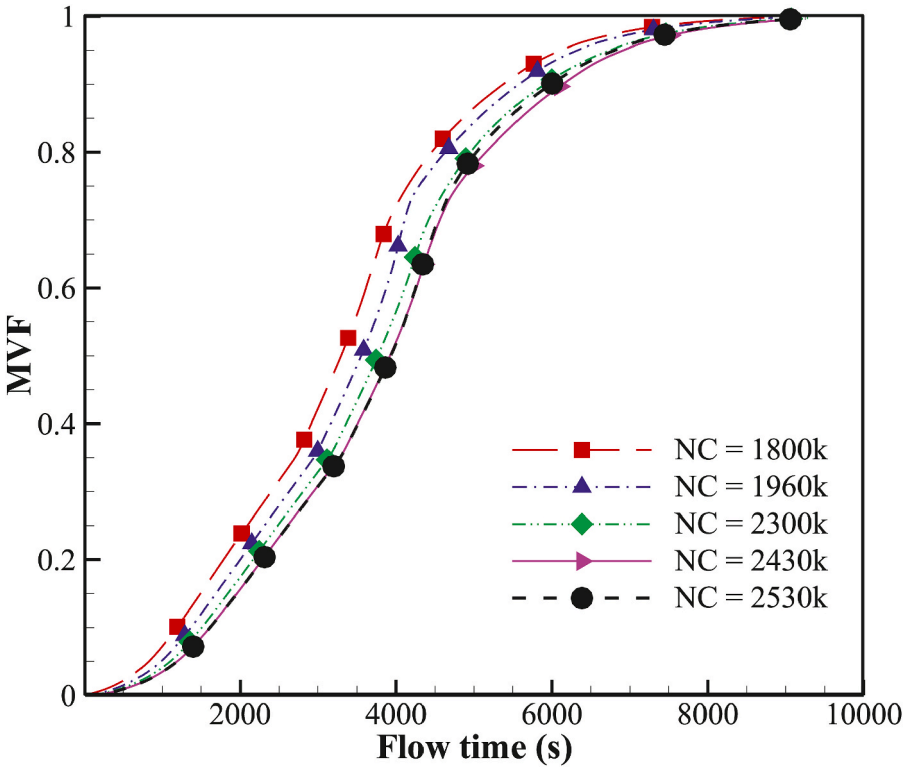


**Fig. 3.** Grid size and accuracy of MVF.

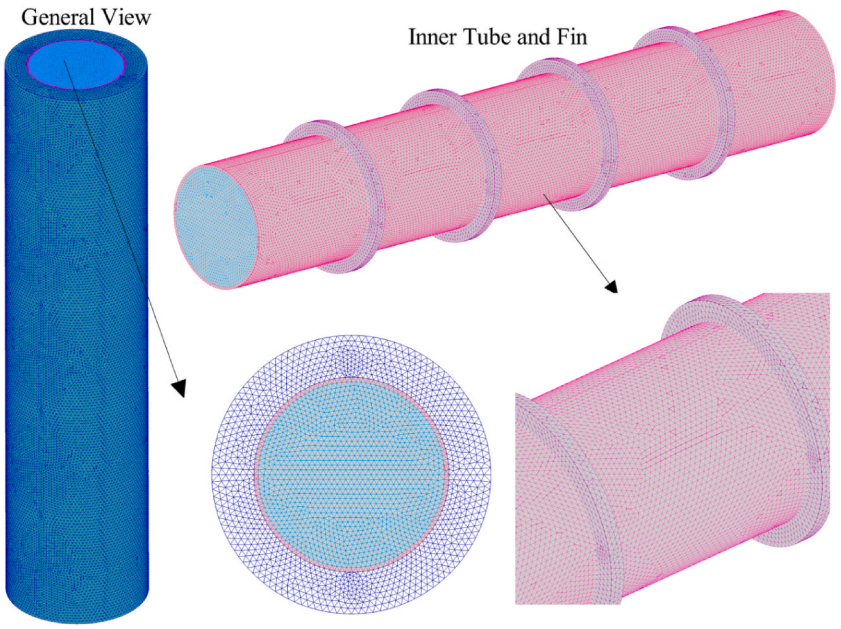


**Fig. 4.** An overview of the chosen grid (NC = 2,430,000).

**Table 2**
Independence from time step for grid 2430k at $t = 6000$s.

| $\Delta t$ = (**Time step** (**s**)) | T (K) | MVF | $Error(\%) = \left\lvert \frac{T_{\Delta t=0.05} - T}{T_{\Delta t=0.05}} \right\rvert \times 100$ | |
|---|---|---|---|---|
| | | | $Error_T$ | $Error_{MVF}$ |
| 0.2 | 308.9 | 0.48 | 2.34 | 46 |
| 0.1 | 313.5 | 0.74 | 0.89 | 16.85 |
| 0.05 | 316.3 | 0.89 | – | – |
| 0.025 | 317.7 | 0.91 | 0.44 | 2.25 |

The empirical data from Kamkari et al. [63], alongside the simulated outcomes of this research, were juxtaposed, particularly in Fig. 5 (a) detailed the temporal progression of temperature at specific locations along a vertical axis at the enclosure's core. Furthermore, Fig. 5 (b), which depicted the MVF and the quantified energy retention throughout the thermal charging process. The

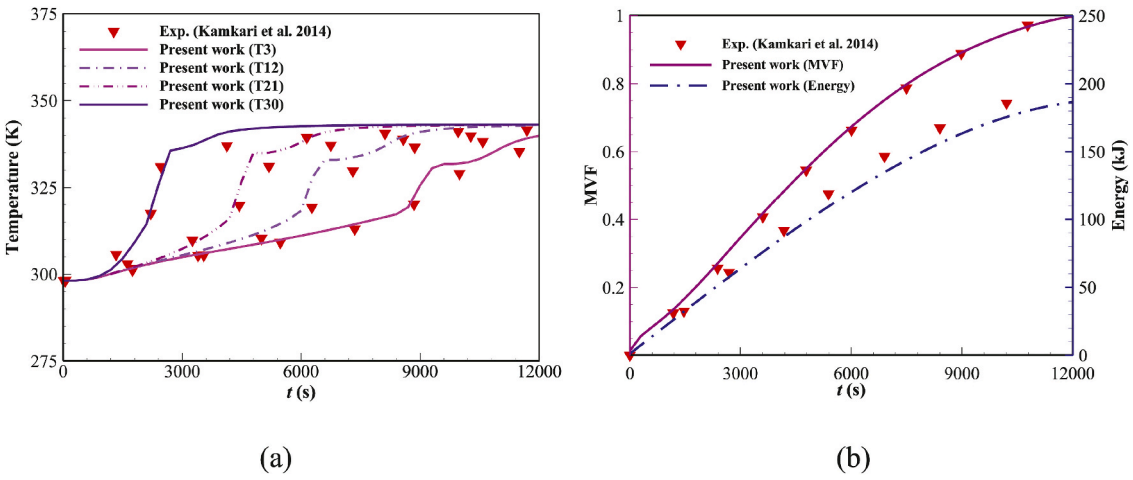


**Fig. 5.** An evaluation contrasting the present research with experimental study [63]: (a) temperature distribution over time, and (b) stored energy and MVF.

concurrence between the observational data and simulation results underscores a significant level of agreement, affirming the simulation's validity and the experimental approach's robustness in capturing the dynamics of melting heat transfer within the specified parameter.

Fig. 6 shows a comparison between the results of the present study and the numerical [64] and experimental [65] studies from the literature for the melting of lauric acid in an enclosure with three fins on the side. The results are captured 45 min after the start of the melting process. As seen, the captured melting interfaces from all studies agree reasonably well. The melting is more advanced in the top regions of the enclosure and next to the top fin, which is due to natural convection effects. The PCM around the fins also melts more effectively because of the heat transfer enhancement provided by the fins.

## 4. Analysis of research findings

The study entailed an investigation aimed at assessing a variety of parameters' effects on the efficacy of a TES. The investigation centred on evaluating the behaviour of molten phase change materials and the incorporation of fins to enhance performance. For this analysis, Case 1, characterized with $w_{i,HWF} = 0.0135$ m/s, $T_{i,HWF} = 323\ K$, $P_{i,PCM} = 10\ Pa$ and $T_{i,PCM} = 323\ K$ was designated as the baseline scenario against which the effects of different parameters were evaluated. According to Table 3, a total of seventeen cases were examined. Specifically, Cases 2 and 3 assessed the influence of pressure, and Cases 4–6 explored how changes in the inlet PCM temperature could affect system performance. The impact of inlet HWF temperature was analyzed in Cases 7 to 9, and Cases 10 to 12 were dedicated to investigating the effect of variations in the velocity of HWF. Finally, Cases 13 to 18 focused on examining how the number and positioning of ports for the introduction and extraction of PCM and HWF influence system efficacy. The outcomes of these assessments are detailed in the subsequent sections of the study.

### 4.1. Effects of PCM inlet pressure

Case 1 is considered as a reference case with $w_{i,HWF} = 0.0135$ m/s, $T_{i,HWF} = 323\ K$, $P_{i,PCM} = 10\ Pa$ and $T_{i,PCM} = 323\ K$. Three other cases with different input pressures of molten PCM ($P_{i,PCM}$) were studied to determine the impact of pressure on the melting fraction. As seen in Fig. 7, $P_{i,PCM}$ has influence on the PCM melting process; So that at a higher pressure (Case 3), the volume fraction of the melt has reached one in a much shorter time. The figure indicates that the difference in cases begins at approximately 3500 s. At this point, the primary PCM liquid film is formed in between the ports of inlet and outlet With an increase in inlet pressure, the melting rate also increases markedly. Most of the differences between the curves are noticeable at around 6000 s, soon after the liquid film forms. Once the liquid film is established, forced convection into the PCM domain starts, and the heated liquid PCM rapidly melts the surrounding PCM. At this stage, the melting speed is limited by the volume of molten PCM entering the latent-heat thermal energy storage unit and the convective exchange between the liquid PCM flow and the solid PCM. Melting slows down toward the end, near 8000 s, as the majority of the solid PCM liquefies, and liquid PCM circulation becomes difficult in the shell's corners. In this situation, higher pressure enhances the flow rate from inlet to outlet but has little effect on the solid PCM in the shell's edges.

### 4.2. Effects of PCM inlet temperature

To determine whether the molten PCM inlet temperature ($T_{i,PCM}$) influences the MVF, three additional cases with varying $T_{i,PCM}$

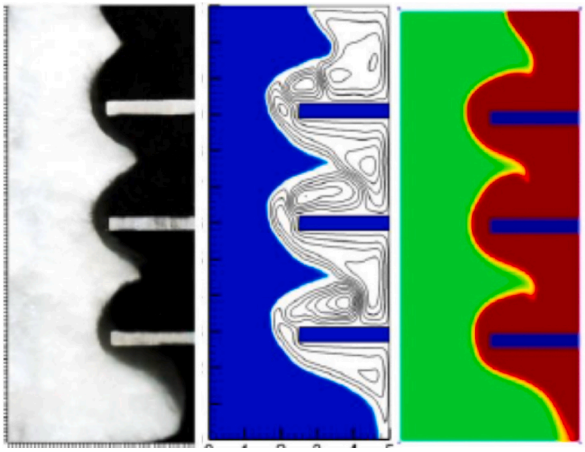

(a) (b) (c)

**Fig. 6.** The comparison of melting interface for (a) experimental measurements of Kamkari and Groulx [65], (b) the numerical studies of Karami and Kamkari [64], and (c) the present simulation of the present study for a three fins placed in lauric acid PCM after 45 min melting.

**Table 3**
The investigated cases have different characteristics regarding the PCM and HWF.

| Case | $P_{i,PCM}$ (Pa) | $T_{i,PCM}$ (K) | $T_{i,HWF}$ (K) | $w_{i,HWF}$ (m/s) | $Port_{i,PCM}$ | $Port_{o,PCM}$ | $L_{i,HWF}$ | $L_{o,HWF}$ | |
|---|---|---|---|---|---|---|---|---|---|
| 1 | 10 | 323 | 323 | 0.0135 | One on top | One on bottom | On bottom | On top | |
| 2 | 5 | 323 | 323 | 0.0135 | One on top | One on bottom | On bottom | On top | |
| 3 | 15 | 323 | 323 | 0.0135 | One on top | One on bottom | On bottom | On top | |
| 4 | 10 | 311 | 323 | 0.0135 | One on top | One on bottom | On bottom | On top | |
| 5 | 10 | 335 | 323 | 0.0135 | One on top | One on bottom | On bottom | On top | |
| 6 | 10 | 359 | 323 | 0.0135 | One on top | One on bottom | On bottom | On top | |
| 7 | 10 | 323 | 311 | 0.0135 | One on top | One on bottom | On bottom | On top | |
| 8 | 10 | 323 | 335 | 0.0135 | One on top | One on bottom | On bottom | On top | |
| 9 | 10 | 323 | 359 | 0.0135 | One on top | One on bottom | On bottom | On top | |
| 10 | 10 | 323 | 323 | 0.0067 | One on top | One on bottom | On bottom | On top | |
| 11 | 10 | 323 | 323 | 0.0201 | One on top | One on bottom | On bottom | On top | |
| 12 | 10 | 323 | 323 | 0.0268 | One on top | One on bottom | On bottom | On top | |
| 13 | 10 | 323 | 323 | 0.0135 | One on top & one on bottom | One on top & one on bottom | On bottom | On top | |
| 14 | 10 | 323 | 323 | 0.0135 | Two on top | Two in bottom | On bottom | On top | |
| 15 | 10 | 323 | 323 | 0.0135 | Two on bottom | Two on top | On bottom | On top | |
| 16 | 10 | 323 | 323 | 0.0135 | One on top | One in bottom | On top | On bottom | |
| 17 | 10 | 323 | 323 | 0.0135 | One on bottom | One on top | On top | On bottom | Four fins |
| 18 | 10 | 323 | 323 | 0.0135 | One on bottom | One on top | On bottom | On top | Four fins |

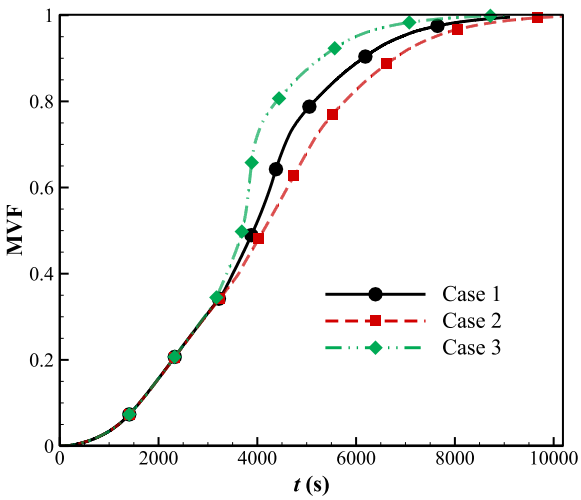


**Fig. 7.** Comparison of MVFs at different $P_{i,PCM}$, with $w_{i,HWF} = 0.0135$ m/s, $T_{i,HWF} = 323\ K$ and $T_{i,PCM} = 323\ K$. Case 1 (10 Pa), Case 2 (5 Pa) and Case 3 (15 Pa).

were analyzed. As seen in Fig. 8, $T_{i,PCM}$ has a clear impact on PCM melting behavior. In Case 6, with $T_{i,PCM} = 359$ K, the PCM reached a fully melted state (MVF = 1.0) in just 6500 s, while the reference case (Case 1, $T_{i,PCM} = 323$ K) required approximately 10,000 s to fully melt. This represents a 35 % reduction in total melting time. At 6000 s, the MVF of Case 6 was 0.999, compared to 0.907 in Case

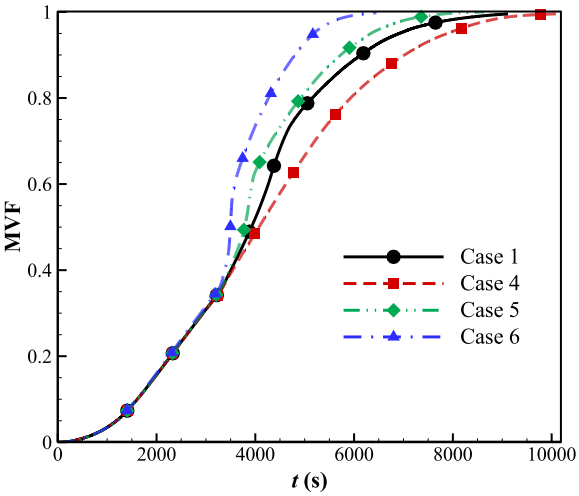


**Fig. 8.** A comparison of MVF at different $T_{i,PCM}$, with $w_{i,HWF} = 0.0135$ m/s, $T_{i,HWF} = 323\,K$ and $P_{i,PCM} = 10\,Pa$. Case 1 ($T_{i,PCM} = 323$ K), Case 4 ($T_{i,PCM} = 311$ K), Case 5 ($T_{i,PCM} = 335$ K), Case 6 ($T_{i,PCM} = 359$ K).

1—indicating an improvement of ~10.1 % in melting progress at that time.

The formation of the initial liquid PCM film is also strongly affected by inlet temperature. The onset of liquid film formation, which begins around 4000 s in Case 4 ($T_{i,PCM} = 311$ K), shifts earlier to 3000 s in Case 6 due to the increased thermal energy delivered through the ports. This earlier onset improves heat transfer to the solid PCM through enhanced conduction. Furthermore, at $t = 6000$ s, Case 5 ($T_{i,PCM} = 335$ K) shows an MVF of 0.935, which is approximately 3 % higher than Case 1. In contrast, Case 4 exhibits a slower melting response with an MVF of 0.824, which is ~9.2 % lower than the reference case.

The melting rate correlates with the temperature difference between the average PCM melting point (308 K) and the inlet PCM temperature. For Cases 4, 1, 5, and 6, these differences are 3 K, 15 K, 27 K, and 51 K, respectively. While a moderate increase in temperature difference (from 3 K to 15 K) improves intermediate-stage melting, it does not substantially shorten total melting time. However, further increases to 27 K and 51 K significantly accelerate both the melting rate and completion time. For instance, Case 6 melts 100 % of the PCM 3500 s faster than the reference, confirming that a higher $T_{i,PCM}$ sharply reduces total melting time and enhances energy transfer, especially near the shell corners where melting is typically delayed.

### 4.3. HWF inlet temperature effects

Three additional cases with varying hot water flow inlet temperatures ($T_{i,HWF}$) were investigated to assess their effect on the melting fraction of the PCM. As shown in Fig. 9, $T_{i,HWF}$ has a pronounced impact on the melting behavior. At 6000 s, Case 7 ($T_{i,HWF} =$

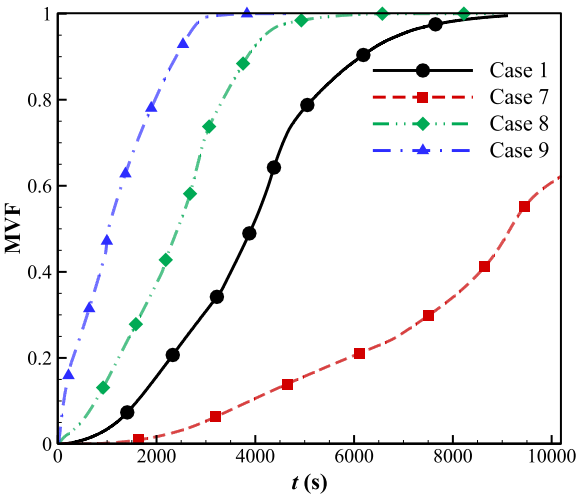


**Fig. 9.** A comparison of MVF at different $T_{i,HWF}$, with $w_{i,HWF} = 0.0135$ m/s, $T_{i,PCM} = 323\,K$ and $P_{i,PCM} = 10\,Pa$. Case 1 ($T_{i,HWF} = 323$ K), Case 7 ($T_{i,HWF} = 311$ K), Case 8 ($T_{i,HWF} = 335$ K), Case 9 ($T_{i,HWF} = 359$ K).

311 K) reached a MVF of 0.208, while Case 1 ($T_{i,HWF}$ = 323 K) reached 0.885. This represents a 325 % increase in MVF when the HWF temperature is raised by just 12 K, highlighting how even modest temperature increases can substantially improve intermediate melting rates. Case 8 ($T_{i,HWF}$ = 335 K) achieved an MVF of 0.993, which is 12.2 % higher than Case 1 at the same time, and 377 % higher than Case 7.

The key mechanism behind this improvement is the expansion of the molten region around the heat source. A higher $T_{i,HWF}$ increases the temperature gradient between the PCM and the HWF, enhancing conductive and convective heat transfer and accelerating the formation of the initial liquid layer that promotes melting.

Additionally, the data show that increasing the inlet temperature from 311 K to 335 K (Case 7 to Case 8) resulted in the MVF rising from 0.208 to 0.993 at 6000 s—an improvement of more than 376 %. This demonstrates how influential $T_{i,HWF}$ is in determining not only the speed of melting but also the spatial uniformity of the melt front. As the hot water flows through the tube, it transfers more heat to the PCM in Cases 8 and 9, leading to faster phase change, especially in the initially slower-melting corners of the shell. These results confirm that optimizing $T_{i,HWF}$ is a highly effective strategy to improve LHTES system performance.

### 4.4. Effects of HWF inlet velocity

To investigate the effect of the inlet velocity of hot water flow ($w_{i,HWF}$) on the melting performance of phase change material (PCM), three additional cases with varying velocities were examined. As shown in Fig. 10, increasing the flow velocity moderately influences the MVF. At 6000 s, Case 10 ($w_{i,HWF}$ = 0.0067 m/s) reached an MVF of 0.8095, while the reference Case 1 ($w_{i,HWF}$ = 0.0135 m/s) achieved 0.8889, showing a 9.8 % improvement in MVF by doubling the inlet velocity. This confirms that increasing the flow rate enhances the heat transfer within the tube and accelerates the melting process, particularly during the early to mid-phase of PCM melting.

Further improvement is observed as the inlet velocity increases. Case 11 ($w_{i,HWF}$ = 0.0201 m/s) reached an MVF of 0.9246, which is about 4 % higher than Case 1 and 14.2 % higher than Case 10 at the same time. Case 12, with the highest velocity of 0.0268 m/s, yielded an MVF of 0.9563, outperforming Case 1 by 7.6 % and Case 10 by 18.1 %. These results highlight that while all cases eventually achieve full melting by around 10,000 s, higher inlet velocities significantly enhance intermediate melting rates, which is particularly valuable in practical applications requiring rapid thermal response. The accelerated heat transfer from the high-speed fluid flow enhances the temperature gradient near the tube surface and promotes faster phase transition in adjacent PCM regions.

However, it is important to note that the benefit of increasing $w_{i,HWF}$ is not linear or unlimited. Although Cases 11 and 12 show higher MVF values at 6000 s, the incremental gain becomes smaller at higher velocities, indicating diminishing returns. Moreover, the shell corners, where heat transfer is dominated by conduction and less affected by tube-side convection, remain a bottleneck for total melting time. Nonetheless, increasing $w_{i,HWF}$ from 0.0067 m/s to 0.0268 m/s results in up to 18 % higher MVF at intermediate times, reducing thermal lag and offering faster energy delivery for thermal energy storage systems. These findings emphasize the importance of optimizing flow velocity to balance performance improvement with energy consumption in LHTES designs.

### 4.5. Effects of the number of PCM ports and HWF flows

An analysis of six different configurations examined the influences of the quantity and positioning PCM ports. Fig. 11 illustrates that among these configurations, Case 13 demonstrated superior performance. This particular setup featured both an input and an output port on the upper surface, as well as on the lower surface of the TES system. Conversely, Cases 15 and 18, which exhibited lower

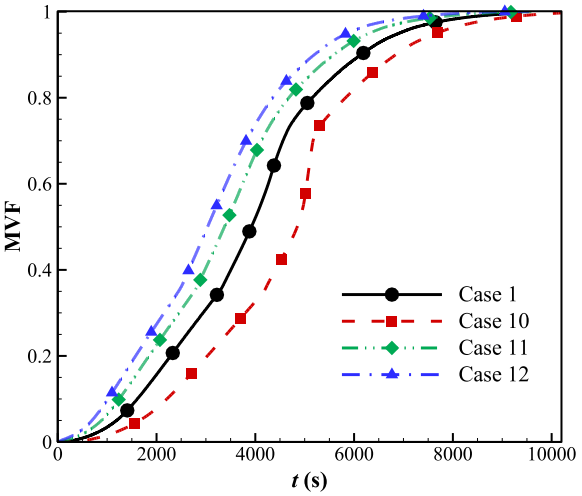


**Fig. 10.** A comparison of MVF at different $w_{i,HWF}$, with $T_{i,PCM}$ = 323 *K* , $T_{i,HWF}$ = 323 *K* and $P_{i,PCM}$ = 10 *Pa*. Case 1 ($w_{i,HWF}$ = 0.0135 m/s), Case 10 ($w_{i,HWF}$ = 0.0067 m/s), Case 11 ($w_{i,HWF}$ = 0.0201 m/s), Case 12 ($w_{i,HWF}$ = 0.0268 m/s).

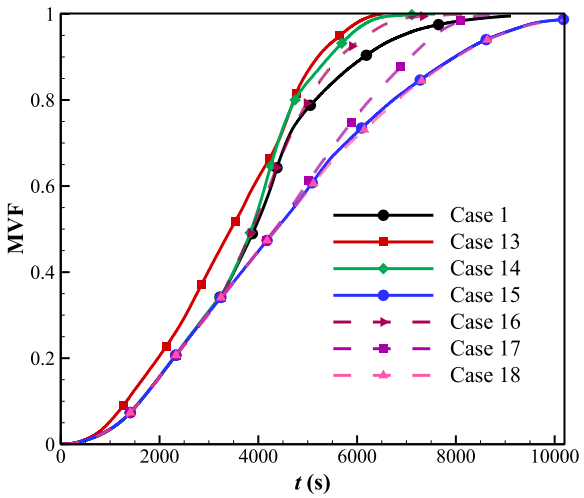


**Fig. 11.** A comparison of MVF with changing the number and direction of the ports.

melting fraction efficiencies, were designed with input ports located on the lower surface (one port in Case 15 and two ports in Case 18) and output ports on the upper surface. It is clear that positioning the input ports on the upper surface enhances performance significantly. Input ports at the top act against natural convection flow and further mix the molten PCM flow within the shell and improve thermal transfer. Conversely, placing input ports on the lower surface, even when increasing their number, does not yield improved performance.

### *4.6. Contours analysis*

In this section, the optimal configurations identified by altering individual parameters in previous analyses are further examined by analyzing melting fraction contours and temperature distributions. Figs. 12–14 assist in this comparison over periods of 3000 and 6000 s.

Fig. 12 details the melting fraction contours at 3000 s for Cases 1, 3, 6, 9, 12, and 13, demonstrating significant improvements in the rate of melting fraction across all scenarios. A particular comparison between Cases 6 and 9 shows that increasing the working fluid's (HWF) inlet temperature significantly surpasses the impact of elevating the inlet PCM temperature in terms of melting efficiency. At 3000 s, Case 12 shows accelerated melting near the fins, suggesting that the velocity of the working fluid also greatly influences the melting process. Due to the strategic placement of PCM inlet ports at both the top and bottom body, Case 13 exhibits an increased melting rate in its lower region.

Fig. 13 illustrates the melting fraction contours at 6000 s for the same cases. In this scenario, Cases 6 and especially Case 9 exhibit much higher melting rates than their counterparts, highlighting the significant impact of higher inlet temperatures on speeding up the melting process. A temperature contour at 3000 and 6000 s in Fig. 14 shows effective heat transfer from the HWF to the fins, facilitating PCM melting.

Table 4 compiles the complete melting times and their improvement percentages over Case 1 to enable a comparative analysis of these optimal cases. Case 9 is the most effective, with a performance enhancement of 64.82 %. This emphasizes the crucial role of working fluid temperature in the melting process, suggesting the possibility of further optimization by introducing hotter working fluids through auxiliary heating mechanisms. Subsequent exergy analysis could evaluate heating solutions regarding their heat contribution, equipment costs, and fuel expenditures. Cases 6 and 13 also show notable improvements, around 30 %, underscoring the importance of PCM temperature and port configuration. Future studies are encouraged to utilize these findings for optimal port placement and to explore strategies for managing PCM inlet temperatures and associated costs.

### *4.7. PCA and neural networks modeling*

Calculating heat transfer during phase transitions requires significant computational power, frequently taking days to complete one case. Due to these heavy requirements, it is typically unfeasible to evaluate numerous models using standard computing systems to assess how design factors influence PCM melting. To better comprehend the behavior of physical systems under varying design conditions, we have integrated Principal Component Analysis (PCA) and Artificial Neural Networks (ANNs) into our approach. This methodology effectively reduces the dimensionality of data, highlighting essential features and reducing extraneous noise, which enhances the interpretability and efficiency of our models. These systems offer effective control settings that influence heat transfer efficiency. Our tailored neural network design features three concealed layers, each containing 15 nodes, and employs a sigmoid activation mechanism. A diagram of the ANN framework is shown in Fig. 15.

Initially, the data undergo normalization and are then processed by PCA, the results of which feed into the ANN. PCA utilizes a

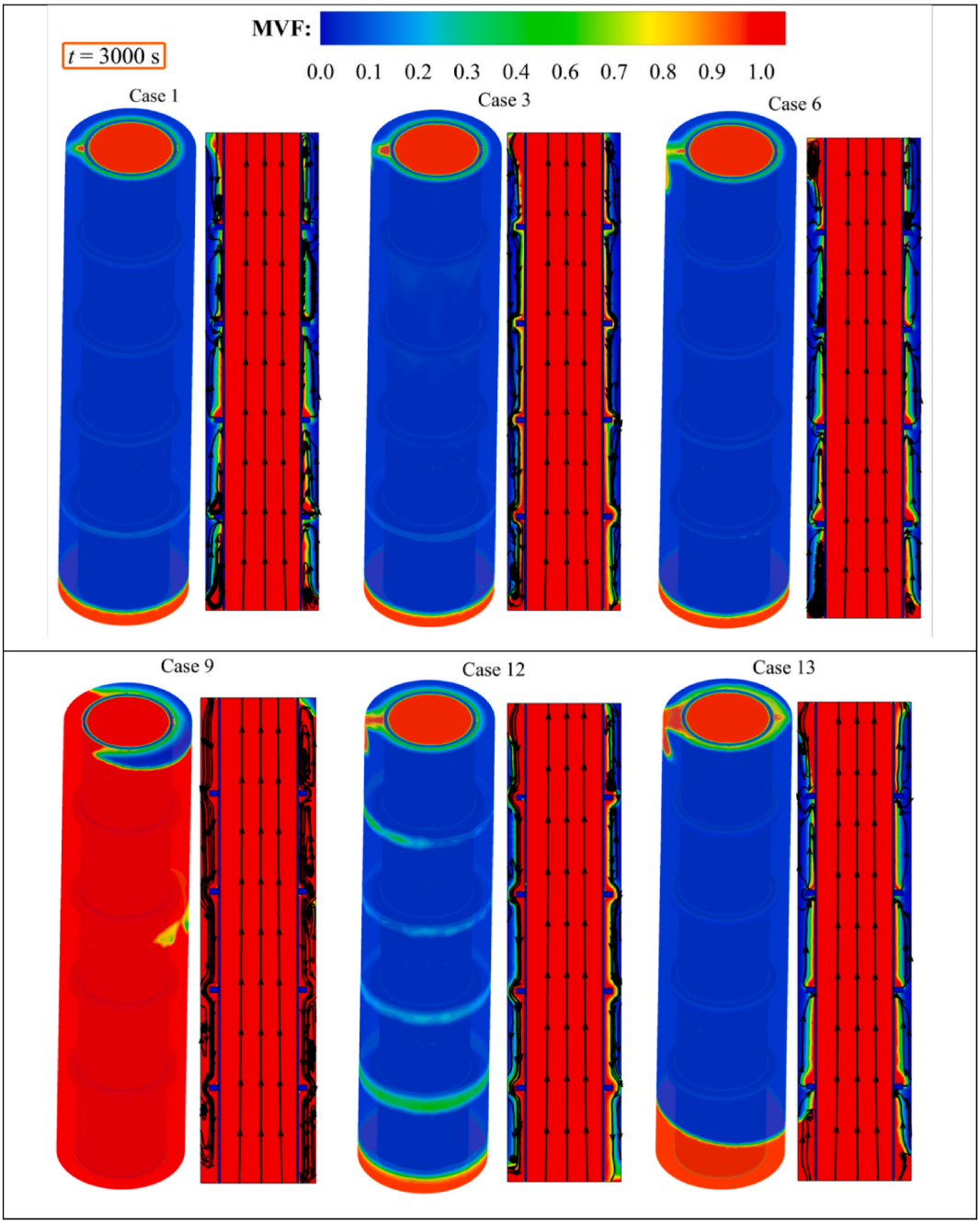


**Fig. 12.** Liquid-fraction contour assessment of optimum cases in each investigated parameter. These contours illustrate for $t = 3000$ s.

randomized SVD solver to efficiently transform the dataset, providing a streamlined input set to the ANN. We have created a dataset from seven distinct melting scenarios, comprising 173,077 simulated data samples. The dataset includes four text-based variables—$Port_{i,PCM}$, $Port_{o,PCM}$, $L_{i,HWF}$, and $L_{o,HWF}$—which we converted into numerical values through label encoding as shown in Table 5, readying them for ANN processing. We have made this dataset publicly accessible: https://doi.org/10.17632/7ht7jcpnjj.1 for future researchers to create or enhance neural network models and conduct deeper outcome analysis. The dataset's inputs and outputs are detailed in Table 6, outlining the range of each parameter, with the complete model illustrated in Fig. 15 and PCA configurations presented in Table 7. Prior to training and using PCA, we normalized the dataset using the StandardScaler method [66] and shuffled it, allocating 70 % for training and the remainder split equally for validation and testing. The normalization process is defined by the equation:

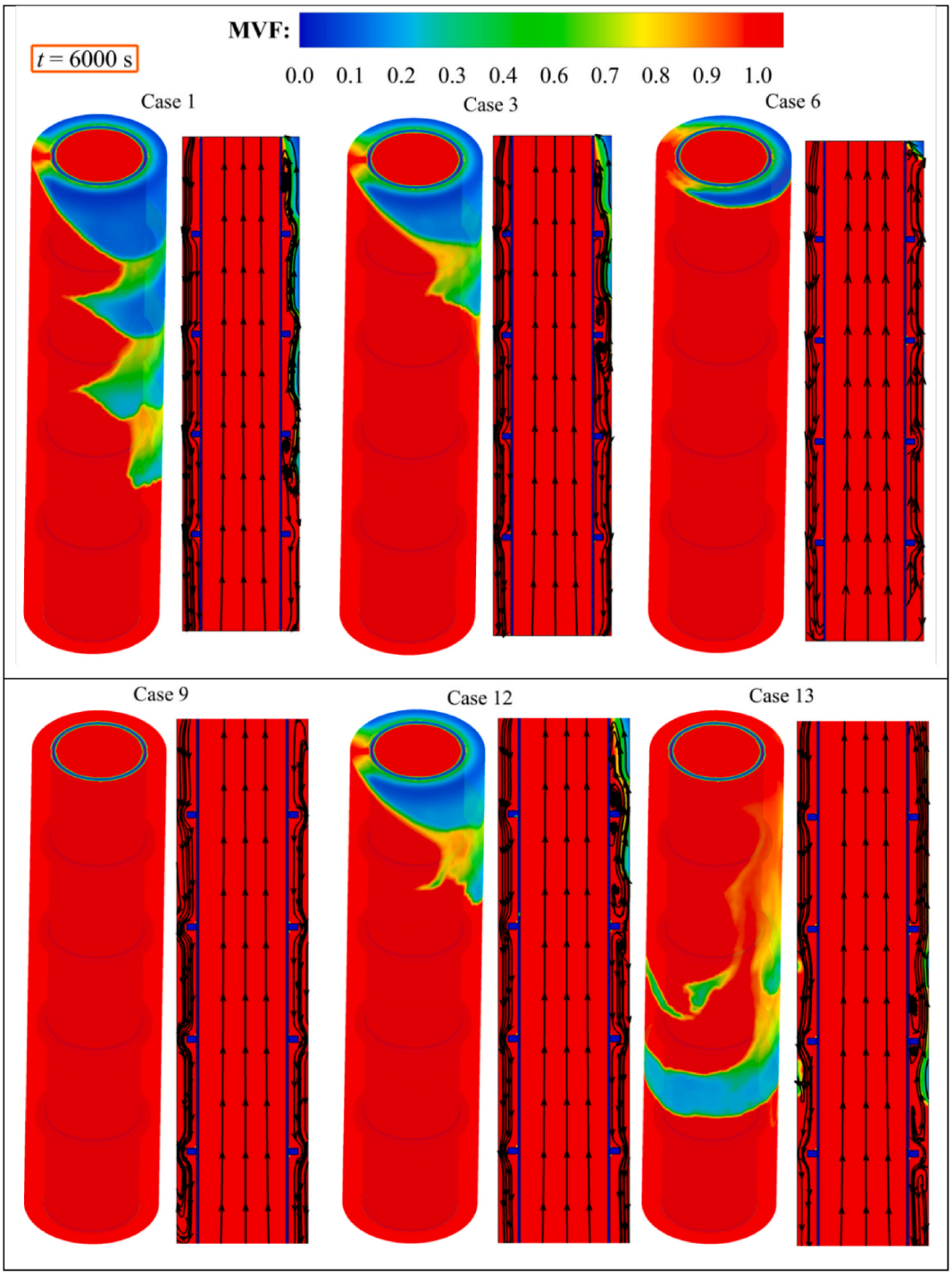


**Fig. 13.** Liquid-fraction contour assessment of optimum cases in each investigated parameter. These contours illustrate $t = 6000$ s.

$$x\_normal = \frac{x - \mu}{\sigma} \tag{5}$$

That $x$ is actual data, $\mu$ is mean of $x$, $\sigma$ is standard deviation of $x$ and $x\_normal$ is normal data.

After normalization, the data are transformed into a new dimension using PCA prior to training, aiming to minimize the Mean Squared Error (MSE) across 1000 iterations with batch sizes of four, using the Adam optimizer. [67]. Post-training, the model showed minute validation and test loss functions at 3.73E-6 and 3.66E-6 respectively, indicating high accuracy. Fig. 16 displays the decreasing

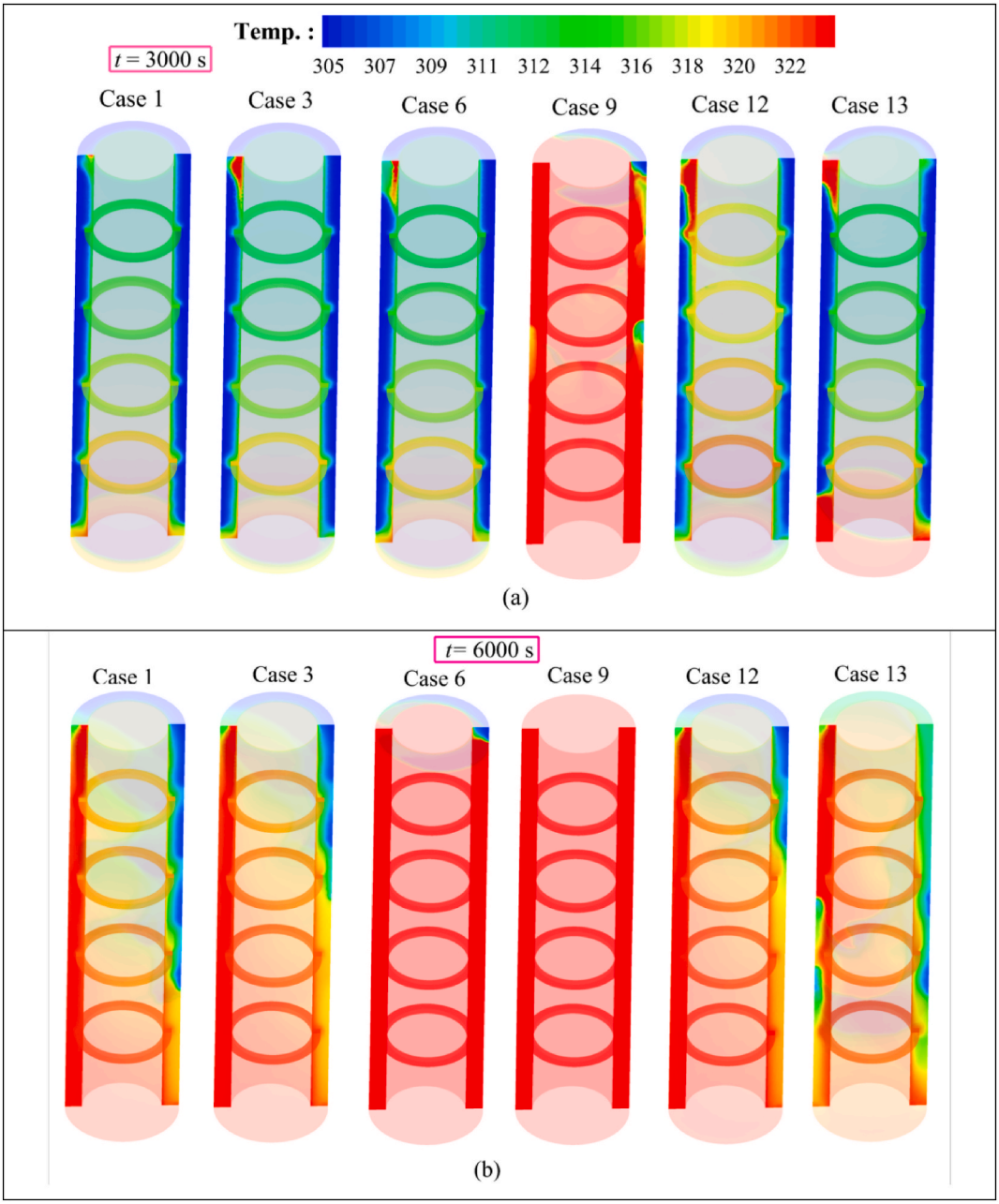


**Fig. 14.** Temperature contour (K) assessment of optimum cases in each investigated parameter. These contours illustrate (a) $t = 3000$ s and (b) $t = 6000$ s.

**Table 4**
Melting time for different investigated configurations.

| Case | MVF time (s) | Comparison of time savings with Case 1 (%) |
|---|---|---|
| 1 | 9117 | – |
| 3 | 9003 | 1.25 |
| 6 | 6207 | 31.91 |
| 9 | 3207 | 64.82 |
| 12 | 7985 | 12.42 |
| 13 | 6259 | 31.35 |

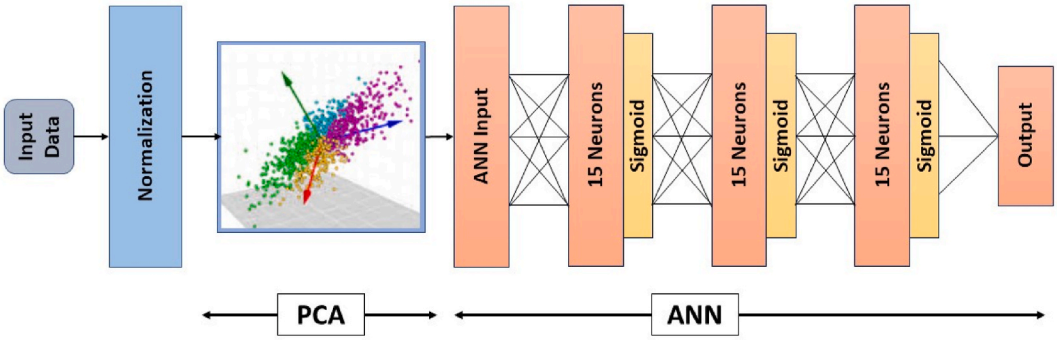


**Fig. 15.** Architectural diagram of the integrated PCA-ANN model for phase change heat transfer analysis.

**Table 5**
Label encoding of textual variables in the PCM melting scenario dataset.

| Variable Name | Actual Value | Assigned number |
|---|---|---|
| $\mathbf{Port_{i,PCM}}$ | One on top | 1 |
| | One on bottom | −1 |
| | Two on top | 2 |
| | Two on bottom | −2 |
| | One on top & one on bottom | 3 |
| $\mathbf{Port_{o,PCM}}$ | One on top | 1 |
| | One on bottom | −1 |
| | Two on top | 2 |
| | Two on bottom | −2 |
| | One on top & one on bottom | 3 |
| $\mathbf{L_{i,HWF}}$ | On bottom | −1 |
| | On top | 1 |
| $\mathbf{L_{o,HWF}}$ | On bottom | −1 |
| | On top | 1 |

**Table 6**
Dataset variables properties.

| Dataset Variables | | |
|---|---|---|
| Symbol | Description | Range |
| *P(i, PCM)* | Inlet pressure of input PCM port (Pa) | 5–15 |
| *T(i, PCM)* | Inlet temperature of input PCM port (K) | 311–359 |
| *T(i, HWF)* | Inlet temperature of hot water flow (K) | 311–359 |
| *w(i, HWF)* | Inlet velocity of hot water flow (m/s) | 0.0067–0.0268 |
| *Port(i,PCM)* | Number and location of PCM input ports | Text_based |
| *Port(o,PCM)* | Number and location of PCM output ports | Text_based |
| *L(i,HWF)* | Input location of the water tube | Text_based |
| *L(o,HWF)* | Output location of the water tube | Text_based |
| *flow_time* | Physical time (s) | 0–10000 |
| *MVF* | Melting volume fraction (−) | 0<MVF<1 |

**Table 7**
PCA Properties according sklearn library of Python [66].

| Setting | Value |
|---|---|
| n_components | None |
| whiten | False |
| svd_solver | Auto |
| tol | 0.0 |
| iterated_power | Auto |
| random_state | None |

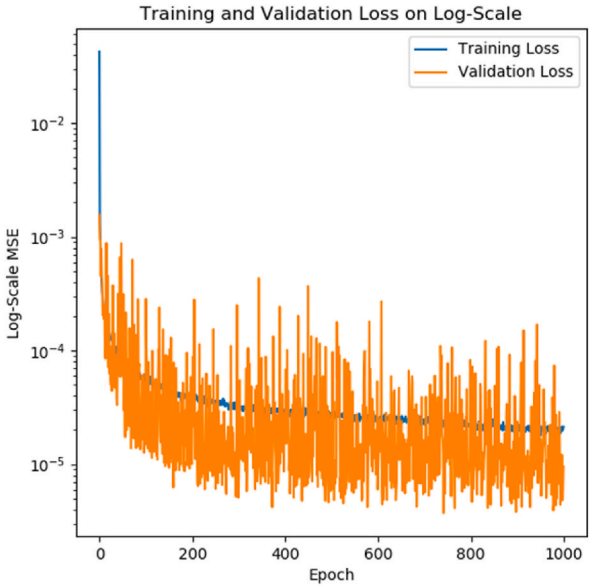


**Fig. 16.** Progression of mean squared error reduction across training and validation epochs.

MSE trend across training process for training and validation data, showing consistent performance improvements. In the meantime, Fig. 17 compares the model's forecasts with real test data, confirming the model's accuracy. These accurate predictions allowed us to generate contour diagrams illustrating the influence of control parameters on the MVF, demonstrating the predictive strength of our hybrid model.

Fig. 18 shows how MVF changes with variations in inlet PCM pressure ($P_{i,PCM}$) and inlet PCM temperature ($T_{i,PCM}$), displayed in contour diagrams. This evaluation focuses on two configurations: a state with an $Port_{i,PCM}$ on top surface of the cylinder and one $Port_{o,PCM}$ at the bottom surface (Fig. 18 ($a_1$), Fig. 18 ($b_1$), and Fig. 18 ($c_1$)); and with one $Port_{i,PCM}$ on the top and one $Port_{i,PCM}$ on the bottom (Fig. 18 ($a_2$), Fig. 18 ($b_2$), and Fig. 18 ($c_2$)). For each arrangement, the MVF was assessed at fixed moments—2500s, 5000s, and 7500s—utilizing ANN. At 2500 s (Fig. 18 ($a_1$) and Fig. 18 ($a_2$)), the MVF ranges from 0.233 to 0.265 in the first configuration and from 0.238 to 0.333 in the second, indicating a positive correlation between MVF, inlet pressure, and temperature. At 5000 s (Fig. 18 ($b_1$) and Fig. 18 ($b_2$)), the MVF spans from 0.62 to 1.0 and 0.81 to 0.9 respectively, showing a significant increase in the molten fraction. By 7500 s (Fig. 18 ($c_1$) and Fig. 18 ($c_2$)), almost the entire unit becomes molten across all configurations.

Fig. 19 illustrates MVF affected by changes in inlet PCM temperature ($T_{i,PCM}$) and inlet hot water temperature ($T_{i,HWF}$), presented

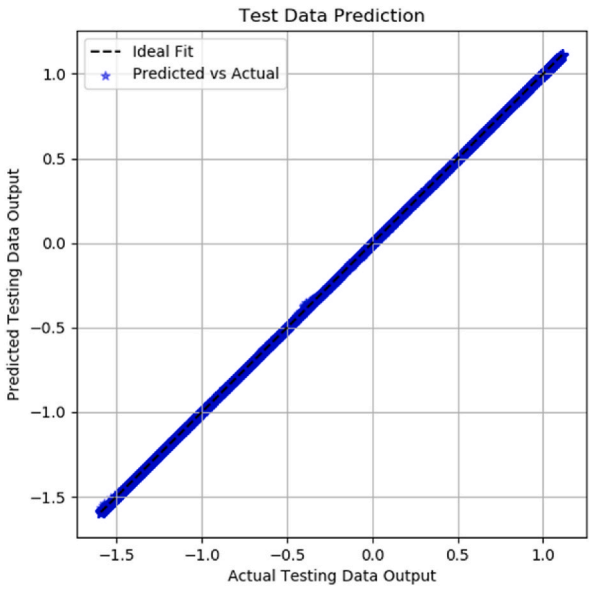


**Fig. 17.** Comparison of predicted vs. actual outcomes for test Data in the PCM model.

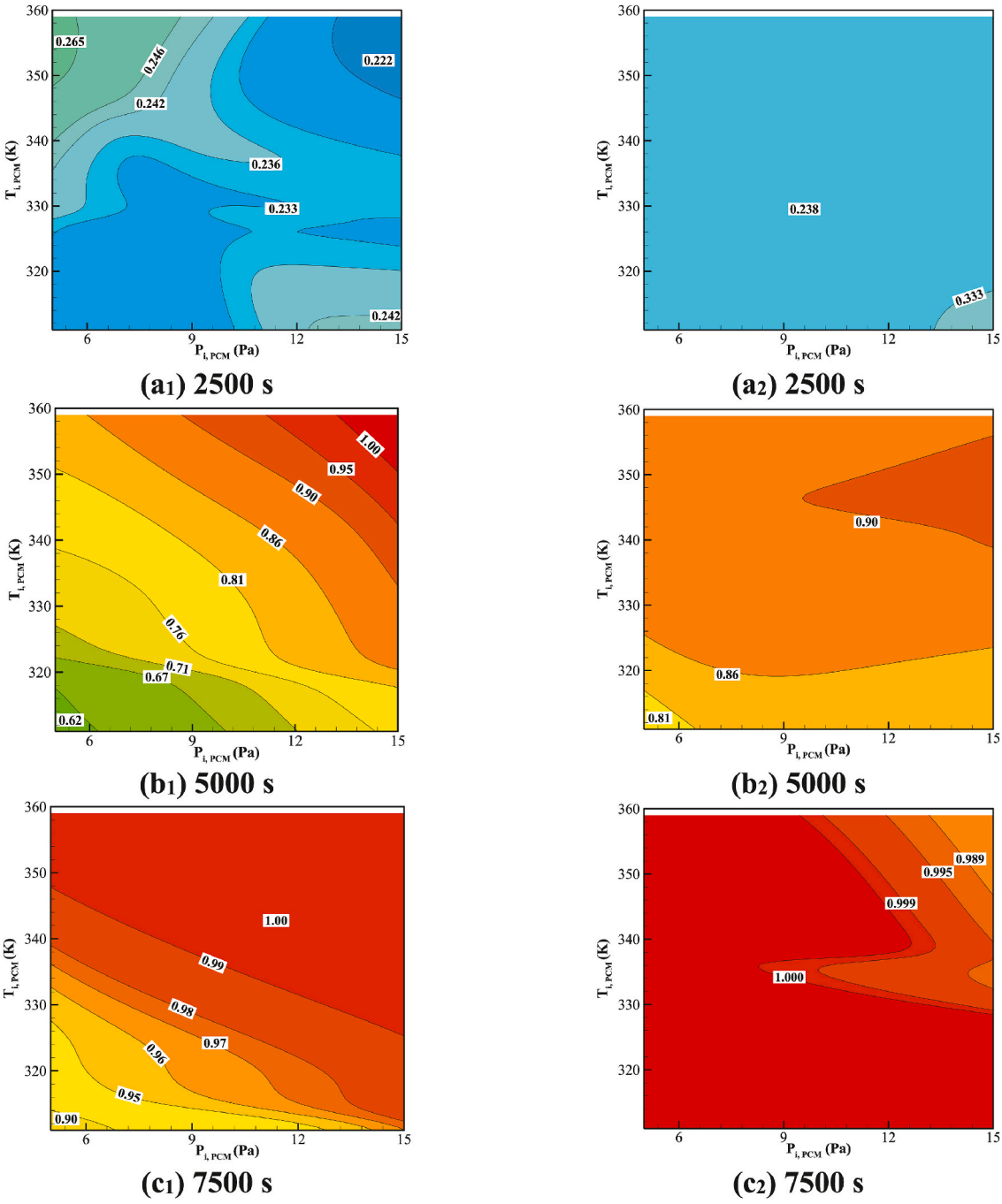


**Fig. 18.** The influence of the inlet PCM temperature ($T_{i,PCM}$) and pressure ($P_{i,PCM}$) on MVF at various times snaps ($a_1$,$b_1$, and $c_1$ are related to the cases with one $Port_{i,PCM}$ on top surface of the cylinder and one $Port_{o,PCM}$ at the bottom surface; $a_2$,$b_2$, and $c_2$ are also related to the cases with One $Port_{i,PCM}$ on the top and one $Port_{i,PCM}$ on the bottom.).

through contour diagrams. This analysis focuses on a configuration with an inlet port on the top surface and an outlet port on the bottom surface. The MVF is calculated at specific intervals—1500s, 3500s, and 6000s—utilizing ANN.

At 1500 s (Fig. 19 (a)), the MVF varies from 0.05 to 0.67, with higher inlet hot water temperatures leading to increased MVF. By 3500 s (Fig. 19 (b)), the MVF ranges from 0.09 to 1.0, with an inlet hot water temperature around 328 K consistently achieving an MVF near 0.9, irrespective of the inlet PCM temperature. At 6000 s (Fig. 19 (c)), cases with an inlet hot water temperature below approximately 325 K exhibit incomplete melting, resulting in unsatisfactory MVF rates.

Fig. 20 depicts the MVF as influenced by variations in inlet hot water temperature ($T_{i,HWF}$) and its velocity ($w_{i,HWF}$), using contour

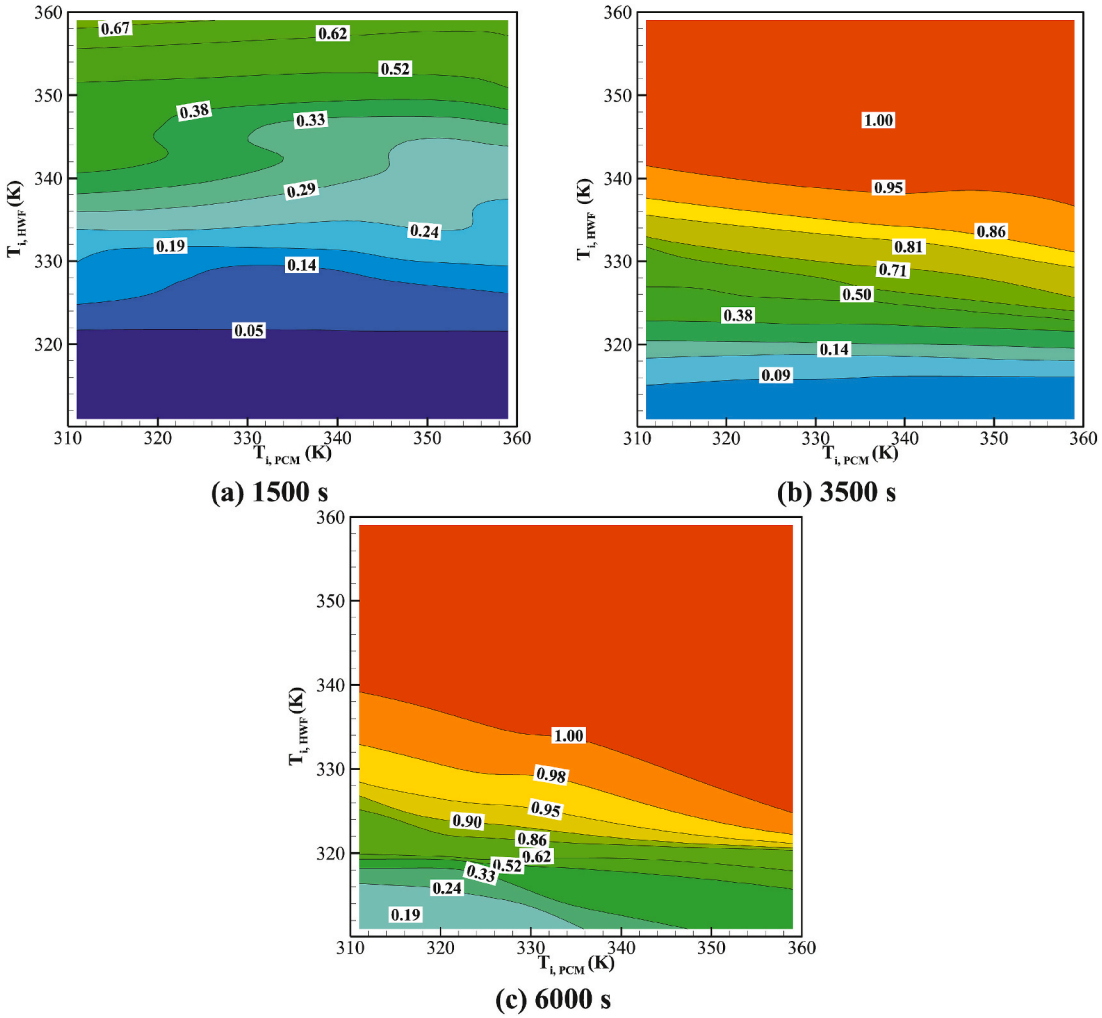


**Fig. 19.** The impact of inlet PCM temperature ($T_{i,PCM}$) and inlet hot water temperature ($T_{i,HWF}$) on MVF at various times snaps.

plots. This analysis considers a configuration with an inlet port on the top surface and an outlet port on the bottom surface. The MVF is calculated at intervals—3000s, 6000s, and 10000s—using a neural network model.

At 3000 s (Fig. 20 (a)), the MVF ranges from 0.05 to 0.76, increasing with higher inlet hot water temperatures and velocity inlet. By 6000 s (Fig. 20 (b)), the MVF spans from 0.19 to 1.0. An inlet hot water temperature of approximately 328 K regularly achieves a MVF close to 0.9, irrespective of the hot water flow rate (velocity). At 10000 s (Fig. 20 (c)), for inlet hot water temperatures of 320 K and above, nearly the entire unit becomes fully molten.

## 5. Conclusions and prospects

This study numerically investigates the dynamic melting of PCM in a finned shell-tube heat exchanger, employing an innovative approach that combines CFD simulation with ANN techniques. The research explored the complex interplay between various operational parameters in a finned LHTES unit, including PCM inlet pressure (5–15 Pa), hot water flow (HWF) inlet temperature (311–359 K), HWF velocities (0.0067–0.0268 m/s), and port configurations. Key findings from this study include:

- HWF inlet temperature significantly impacted melting rates. Case 9, with the highest HWF inlet temperature of 359 K, exhibited a remarkable 64.82 % improvement in melting rate compared to the baseline case. The enhanced performance can be attributed to the increased temperature gradient between the HWF and PCM, leading to more rapid heat transfer and consequently faster melting.
- Optimization of PCM temperature and port configuration, as demonstrated in Cases 6 and 13, yielded approximately 30 % enhancement in system performance. Case 6, with a PCM inlet temperature of 335 K, showed improved heat transfer characteristics due to the reduced temperature difference between the incoming PCM and the melting point (311 K for RT35).

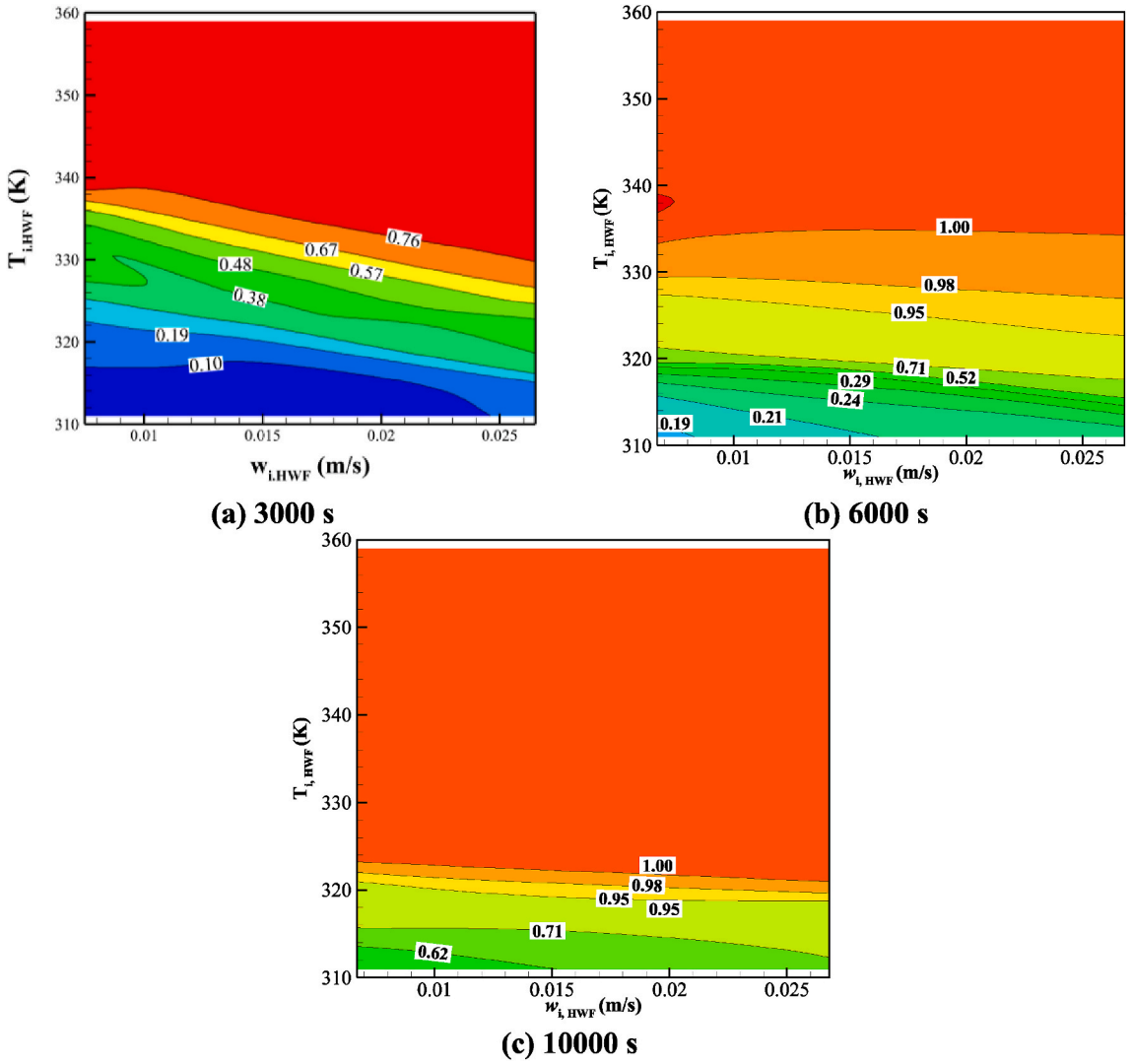


**Fig. 20.** The impact of inlet hot water temperature ($T_{i,HWF}$) and its velocity ($w_{i,HWF}$) on MVF at various times snaps.

- Higher inlet temperatures not only promoted more uniform melting but also significantly reduced melting time. For instance, increasing the HWF inlet temperature from 311 K to 359 K reduced the total melting time by 58.3 %. This improvement is likely due to enhanced natural convection within the liquid PCM, facilitated by the greater temperature gradient.
- The ANN model, constructed with 70 % of the data for training, 15 % for validation, and 15 % for testing, demonstrated high accuracy in predicting system performance. It achieved a correlation coefficient (R) of 0.9988 and a mean squared error (MSE) of 0.0047, proving its efficacy as a rapid assessment tool for LHTES system optimization. The model employed a feed-forward backpropagation algorithm with a Levenberg-Marquardt training function and a hyperbolic tangent sigmoid transfer function.
- The CFD simulations revealed that the liquid fraction of PCM increased non-linearly with time, with the rate of increase being highest in the initial stages of melting. For instance, in Case 9, 50 % of the PCM melted within the first 30 % of the total melting time, indicating the importance of initial heat transfer rates.

The integration of dynamic melting techniques with fin-assisted heat transfer presents a promising hybrid enhancement strategy for LHTES systems. This approach offers significant potential for improving thermal efficiency without compromising the PCM volume, addressing a key limitation of traditional enhancement methods. Future research directions should focus on:

a. Exploring more complex fin geometries, such as tree-like or fractal structures, and their interaction with dynamic melting processes to further optimize heat transfer.
b. Investigating the long-term stability and performance of dynamically melted PCM systems, particularly focusing on potential issues like thermal cycling fatigue and PCM segregation.

c. Extending the CFD-ANN model to incorporate multi-objective optimization, considering factors such as energy efficiency, cost, and system compactness simultaneously.

## CRediT authorship contribution statement

**Fathi Alimi:** Writing – original draft, Resources, Methodology, Investigation, Conceptualization. **Nashmi H. Alrasheedi:** Writing – review & editing, Supervision, Resources, Project administration, Investigation, Funding acquisition. **Mohammad Edalatifar:** Writing – original draft, Visualization, Software, Methodology, Data curation, Conceptualization. **Jana Shafi:** Writing – original draft, Visualization, Software, Formal analysis, Data curation. **Khalil Hajlaoui:** Writing – review & editing, Writing – original draft, Validation, Resources, Methodology, Investigation. **Saleh Chebaane:** Writing – review & editing, Writing – original draft, Methodology, Investigation, Formal analysis. **Mohamed Bouzidi:** Writing – review & editing, Writing – original draft, Project administration, Methodology. **Mehdi Ghalambaz:** Writing – review & editing, Writing – original draft, Visualization, Validation, Supervision, Conceptualization.

## Funding statement

This work was supported and funded by the Deanship of Scientific Research at Imam Mohammad Ibn Saud Islamic University (IMSIU) (grant number IMSIU-DDRSP2503).

## Declaration of competing interest

The authors clarify that there is no conflict of interest for report.

## Data availability

Data is available here: https://doi.org/10.17632/7ht7jcpnjj.1.

## References

[1] S. Zhang, D. Feng, L. Shi, L. Wang, Y. Jin, L. Tian, Z. Li, G. Wang, L. Zhao, Y. Yan, A review of phase change heat transfer in shape-stabilized phase change materials (ss-PCMs) based on porous supports for thermal energy storage, Renew. Sustain. Energy Rev. 135 (2021).
[2] W. Liu, Y. Bie, T. Xu, A. Cichon, G. Królczyk, Z. Li, Heat transfer enhancement of latent heat thermal energy storage in solar heating system: a state-of-the-art review, J. Energy Storage 46 (2022).
[3] S. Nishad, M. Ouederni, I. Krupa, Thermal energy storage materials designed from recycled Tetra Pak waste and paraffin waxes with enhanced photothermal conversion efficiencies, Energy Built Environ. 6 (3) (2025) 455–465.
[4] S. Rostami, M. Afrand, A. Shahsavar, M. Sheikholeslami, R. Kalbasi, S. Aghakhani, M.S. Shadloo, H.F. Oztop, A review of melting and freezing processes of PCM/nano-PCM and their application in energy storage, Energy 211 (2020).
[5] I. Mechai, A. Almarashi, W. Hamali, M.Y. Almusawa, R. Qahiti, H.A. Al-Bonsrulah, N.B. Elbashir, Simulation of integration of photovoltaic solar system with storage unit incorporating mixture of paraffin and nanoparticles, J. Energy Storage 82 (2024) 110513.
[6] F.L. Rashid, M.A. Al-Obaidi, A. Dulaimi, L.F.A. Bernardo, Z.A.A. Redha, H.A. Hoshi, H.B. Mahood, A. Hashim, Recent advances on the applications of phase change materials in cold thermal energy storage: a critical review, J. Compos. Sci. 7 (2023) 338.
[7] H. Togun, H.S. Sultan, H.I. Mohammed, A.M. Sadeq, N. Biswas, H.A. Hasan, R.Z. Homod, A.H. Abdulkadhim, Z.M. Yaseen, P. Talebizadehsardari, A critical review on phase change materials (PCM) based heat exchanger: different hybrid techniques for the enhancement, J. Energy Storage 79 (2024) 109840.
[8] Z.A. Qureshi, H.M. Ali, S. Khushnood, Recent advances on thermal conductivity enhancement of phase change materials for energy storage system: a review, Int. J. Heat Mass Tran. 127 (2018) 838–856.
[9] J.M. Mahdi, S. Lohrasbi, E.C. Nsofor, Hybrid heat transfer enhancement for latent-heat thermal energy storage systems: a review, Int. J. Heat Mass Tran. 137 (2019) 630–649.
[10] F.L. Rashid, N.S. Dhaidan, A.J. Mahdi, H.N. Azziz, R. Parveen, H. Togun, R.Z. Homod, Heat transfer enhancement of phase change materials using letters-shaped fins: a review, Int. Commun. Heat Mass Tran. 159 (2024) 108096.
[11] F.L. Rashid, A. Basem, F.A.A. Khalaf, M.H. Abbas, A. Hashim, Recent breakthroughs and improvements in phase change material melting in a triple-tube thermal storage unit, Rev. Compos. Matériaux Avancés 32 (2022) 295.
[12] F.L. Rashid, H.I. Mohammed, A. Dulaimi, M.A. Al-Obaidi, P. Talebizadehsardari, S. Ahmad, A. Ameen, Analysis of heat transfer in various cavity geometries with and without nano-enhanced phase change material: a review, Energy Rep. 10 (2023) 3757–3779.
[13] F.L. Rashid, A.F. Khalaf, M.A. Al-Obaidi, A. Dulaimi, A. Ameen, Investigating the impact of cell inclination on phase change material melting in square cells: a numerical study, Materials 17 (2024) 633.
[14] D. Jayathunga, H. Karunathilake, M. Narayana, S. Witharana, Phase change material (PCM) candidates for latent heat thermal energy storage (LHTES) in concentrated solar power (CSP) based thermal applications-A review, Renew. Sustain. Energy Rev. 189 (2024) 113904.
[15] Z. Omara, M.M. Ahmed, W.H. Alawee, S. Shanmugan, M. Elashmawy, A comprehensive review of nano-enhanced phase change materials on solar stills with scientometric analysis, Results Eng. (2024) 102088.
[16] S.E. Ahmed, A. Abderrahmane, S. Alotaibi, O. Younis, R.A. Almasri, W.K. Hussam, Enhanced heat transfer for NePCM-melting-based thermal energy of finned heat pipe, Nanomaterials 12 (2021) 129.
[17] A. Belazreg, A. Abderrahmane, N.A. Qasem, N. Sene, S. Mohammed, O. Younis, K. Guedri, N. Nasajpour-Esfahani, D. Toghraie, Effect of Y-shaped fins on the performance of shell-and-tube thermal energy storage unit, Case Stud. Therm. Eng. 40 (2022) 102485.
[18] J. Shi, H. Du, Z. Chen, S. Lei, Review of phase change heat transfer enhancement by metal foam, Appl. Therm. Eng. 219 (2023) 119427.
[19] M. Ghalambaz, M. Aljaghtham, A.J. Chamkha, A. Abdullah, A. Alshehri, M. Ghalambaz, Anisotropic metal foam design for improved latent heat thermal energy storage in a tilted enclosure, Int. J. Mech. Sci. 238 (2023) 107830.
[20] A. Abderrahmane, M. Al-Khaleel, A. Mourad, H. Laidoudi, Z. Driss, O. Younis, K. Guedri, R. Marzouki, Natural convection within inversed T-shaped enclosure filled by nano-enhanced phase change material: numerical investigation, Nanomaterials 12 (2022) 2917.
[21] W. Al-Kouz, A. Aissa, S.S.U. Devi, M. Prakash, L. Kolsi, H. Moria, W. Jamshed, O. Younis, Effect of a rotating cylinder on the 3D MHD mixed convection in a phase change material filled cubic enclosure, Sustain. Energy Technol. Assessments 51 (2022) 101879.

[22] L. Pu, S. Zhang, L. Xu, Y. Li, Thermal performance optimization and evaluation of a radial finned shell-and-tube latent heat thermal energy storage unit, Appl. Therm. Eng. 166 (2020) 114753.
[23] Z.H. Low, Z. Qin, F. Duan, A review of fin application for latent heat thermal energy storage enhancement, J. Energy Storage 85 (2024) 111157.
[24] H.S. Sultan, H.I. Mohammed, N. Biswas, H. Togun, R.K. Ibrahem, J.M. Mahdi, W. Yaïci, A. Keshmiri, P. Talebizadehsardari, Revolutionizing the latent heat storage: boosting discharge performance with innovative undulated phase change material containers in a vertical shell-and-tube system, J. Comput. Design Eng. 11 (2024) 122–145.
[25] N.B. Khedher, H. Togun, H.S.S. Aljibori, H.I. Mohammed, K. Khosravi, A.M. Abed, M. Boujelbene, J.M. Mahdi, Accelerated melting dynamics in latent-heat storage systems via longitudinal and circular fins: a comprehensive 3D analysis, Int. Commun. Heat Mass Tran. 156 (2024) 107602.
[26] S. Almsater, W. Saman, F. Bruno, Numerical investigation of PCM in vertical triplex tube thermal energy storage system for CSP applications, in: AIP Conference Proceedings, AIP Publishing, 2017.
[27] M.K. Rathod, J. Banerjee, Thermal performance enhancement of shell and tube latent heat storage unit using longitudinal fins, Appl. Therm. Eng. 75 (2015) 1084–1092.
[28] J.M. Mahdi, E.C. Nsofor, Solidification of a PCM with nanoparticles in triplex-tube thermal energy storage system, Appl. Therm. Eng. 108 (2016) 596–604.
[29] X. Yang, J. Guo, B. Yang, H. Cheng, P. Wei, Y.-L. He, Design of non-uniformly distributed annular fins for a shell-and-tube thermal energy storage unit, Appl. Energy 279 (2020).
[30] M. Boujelbene, J.M. Mahdi, H.S. Sultan, R.Z. Homod, A. Yvaz, I.S. Chatroudi, P. Talebizadehsardari, The potential of arc-shaped fins for expedited solidification in triplex-tube latent heat storage: parametric investigation, J. Build. Eng. 82 (2024) 108176.
[31] N.B. Khedher, H. Togun, A.M. Abed, H.I. Mohammed, J.M. Mahdi, R.K. Ibrahem, W. Yaïci, P. Talebizadehsardari, A. Keshmiri, Comprehensive analysis of melting enhancement by circular Y-shaped fins in a vertical shell-and-tube heat storage system, Eng. Appl. Comput. Fluid Mech. 17 (2023) 2227682.
[32] C. Ji, Z. Qin, S. Dubey, F.H. Choo, F. Duan, Simulation on PCM melting enhancement with double-fin length arrangements in a rectangular enclosure induced by natural convection, Int. J. Heat Mass Tran. 127 (2018) 255–265.
[33] I. Jmal, M. Baccar, Numerical investigation of PCM solidification in a finned rectangular heat exchanger including natural convection, Int. J. Heat Mass Tran. 127 (2018) 714–727.
[34] F. Agyenim, P. Eames, M. Smyth, A comparison of heat transfer enhancement in a medium temperature thermal energy storage heat exchanger using fins, Sol. Energy 83 (2009) 1509–1520.
[35] A.H. Mosaffa, C.A. Infante Ferreira, F. Talati, M.A. Rosen, Thermal performance of a multiple PCM thermal storage unit for free cooling, Energy Convers. Manag. 67 (2013) 1–7.
[36] A. Sciacovelli, F. Gagliardi, V. Verda, Maximization of performance of a PCM latent heat storage system with innovative fins, Appl. Energy 137 (2015) 707–715.
[37] J.R. Patel, M.K. Rathod, Thermal performance enhancement of melting and solidification process of phase-change material in triplex tube heat exchanger using longitudinal fins, Heat Tran. Asian Res. 48 (2018) 483–501.
[38] A.A. Al-Abidi, S. Mat, K. Sopian, M.Y. Sulaiman, A.T. Mohammad, Numerical study of PCM solidification in a triplex tube heat exchanger with internal and external fins, Int. J. Heat Mass Tran. 61 (2013) 684–695.
[39] A. Sharma, P.K. Singh, E. Makki, J. Giri, T. Sathish, A comprehensive review of critical analysis of biodegradable waste PCM for thermal energy storage systems using machine learning and deep learning to predict dynamic behavior, Heliyon 10 (2024) e25800.
[40] H.S. Sultan, M.H. Ali, J. Shafi, M. Fteiti, M. Baro, F. Alresheedi, M.S. Islam, T. Yusaf, M. Ghalambaz, Improving phase change heat transfer in an enclosure filled by uniform and heterogenous metal foam layers: a neural network design approach, J. Energy Storage 85 (2024) 110954.
[41] E. Thangapandian, P. Palanisamy, S.K. Selvaraj, U. Chadha, M. Khanna, Detailed experimentation and prediction of thermophysical properties in lauric acid-based nanocomposite phase change material using artificial neural network, J. Energy Storage 74 (2023) 109345.
[42] A. Maalla, M. Dahari, R. Chaturvedi, Y. Fouad, S. Abdullaev, A. Farag, A. Alkhayyat, G.M. Abdo, Artificial neural network-based optimization of heat absorption process of phase change materials in a novel-designed finned-plate latent heat storage system, J. Energy Storage 86 (2024) 111256.
[43] N.H.S. Tay, M. Liu, M. Belusko, F. Bruno, Review on transportable phase change material in thermal energy storage systems, Renew. Sustain. Energy Rev. 75 (2017) 264–277.
[44] Y. Kozak, T. Rozenfeld, G. Ziskind, Close-contact melting in vertical annular enclosures with a non-isothermal base: theoretical modeling and application to thermal storage, Int. J. Heat Mass Tran. 72 (2014) 114–127.
[45] J.J. Vadasz, J.P. Meyer, S. Govender, G. Ziskind, Experimental study of vibration effects on heat transfer during solidification of paraffin in a spherical shell, Exp. Heat Transf. 29 (2015) 285–298.
[46] F. Hu, D.-W. Sun, W. Gao, Z. Zhang, X. Zeng, Z. Han, Effects of pre-existing bubbles on ice nucleation and crystallization during ultrasound-assisted freezing of water and sucrose solution, Innov. Food Sci. Emerg. Technol. 20 (2013) 161–166.
[47] V. Zipf, A. Neuhäuser, D. Willert, P. Nitz, S. Gschwander, W. Platzer, High temperature latent heat storage with a screw heat exchanger: design of prototype, Appl. Energy 109 (2013) 462–469.
[48] W.-M. Yan, K.-E. Gao, U. Sajjad, L.-H. Chien, M. Amani, Experimental study of dynamic melting process in an ice-on-coil storage system, J. Energy Storage 73 (2023).
[49] B. He, F. Setterwall, Technical grade paraffin waxes as phase change materials for cool thermal storage and cool storage systems capital cost estimation, Energy Convers. Manag. 43 (2002) 1709–1723.
[50] N.H.S. Tay, F. Bruno, M. Belusko, Experimental investigation of dynamic melting in a tube-in-tank PCM system, Appl. Energy 104 (2013) 137–148.
[51] N.H.S. Tay, M. Belusko, M. Liu, F. Bruno, Investigation of the effect of dynamic melting in a tube-in-tank PCM system using a CFD model, Appl. Energy 137 (2015) 738–747.
[52] J. Gasia, D. Groulx, N.H.S. Tay, L.F. Cabeza, Numerical study of dynamic melting enhancement in a latent heat thermal energy storage system, J. Energy Storage 31 (2020).
[53] S. Sajadian, K. Hosseinzadeh, S. Akbari, A. Rahbari, P. Talebizadehsardari, A. Keshmiri, Discharge optimization in shell-and-tube latent heat storage systems using response surface methodology, Results Eng. 25 (2025) 104157.
[54] S. Ebadi, M. Al-Jethelah, S.H. Tasnim, S. Mahmud, An investigation of the melting process of RT-35 filled circular thermal energy storage system, Open Phys. 16 (2018) 574–580.
[55] H. Zheng, C. Wang, Q. Liu, Z. Tian, X. Fan, Thermal performance of copper foam/paraffin composite phase change material, Energy Convers. Manag. 157 (2018) 372–381.
[56] F. Alimi, H.S.S. Aljibori, M. Bouzidi, A. Alasmari, S. Yazdani, M. Ghalambaz, Improving a shell-tube latent heat thermal energy storage unit for building hot water demand using metal foam inserts at a constant pumping power, J. Build. Eng. 98 (2024) 111040.
[57] S.-K. Choi, S.-O. Kim, T.-H. Lee, Dohee-Hahn, Computation of the natural convection of nanofluid in a square cavity with homogeneous and nonhomogeneous models, Numer. Heat Transf. A Appl. 65 (2014) 287–301.
[58] F.T. Najim, H.I. Mohammed, H.M.T. Al-Najjar, L. Thangavelu, M.Z. Mahmoud, J.M. Mahdi, M.E. Tiji, W. Yaïci, P. Talebizadehsardari, Improved melting of latent heat storage using fin arrays with non-uniform dimensions and distinct patterns, Nanomaterials 12 (2022) 403.
[59] P. Wang, X. Wang, Y. Huang, C. Li, Z. Peng, Y. Ding, Thermal energy charging behaviour of a heat exchange device with a zigzag plate configuration containing multi-phase-change-materials (m-PCMs), Appl. Energy 142 (2015) 328–336.
[60] J. Blazek, Principles of solution of the governing equations, in: J. Blazek (Ed.), Computational Fluid Dynamics: Principles and Applications, third ed., 2015, pp. 121–166.
[61] M.E. Tiji, S. Rezaei, K. Hosseinzadeh, S. Kaplan, P. Talebizadehsardari, A. Keshmiri, Optimizing heat transfer in a finned rectangular latent heat storage system using response surface methodology, Case Stud. Therm. Eng. 66 (2025) 105701.
[62] M. Ghalambaz, H.I. Mohammed, A. Naghizadeh, M.S. Islam, O. Younis, J.M. Mahdi, I.S. Chatroudi, P. Talebizadehsardari, Optimum placement of heating tubes in a multi-tube latent heat thermal energy storage, Materials 14 (2021) 1232.

[63] B. Kamkari, H. Shokouhmand, F. Bruno, Experimental investigation of the effect of inclination angle on convection-driven melting of phase change material in a rectangular enclosure, Int. J. Heat Mass Tran. 72 (2014) 186–200.
[64] R. Karami, B. Kamkari, Investigation of the effect of inclination angle on the melting enhancement of phase change material in finned latent heat thermal storage units, Appl. Therm. Eng. 146 (2019) 45–60.
[65] B. Kamkari, D. Groulx, Experimental investigation of melting behaviour of phase change material in finned rectangular enclosures under different inclination angles, Exp. Therm. Fluid Sci. 97 (2018) 94–108.
[66] Scikit-learn, sklearn.preprocessing.StandardScaler, in: Scikit-Learn, 2023.
[67] I.K.M. Jais, A.R. Ismail, S.Q. Nisa, Adam optimization algorithm for wide and deep neural network, Knowledge Eng. Data Sci. 2 (2019) 41–46.